

## MIT Open Access Articles

*A newly developed APCC SCoPS and its prediction  
of East Asia seasonal climate variability*

The MIT Faculty has made this article openly available. **Please share**  
how this access benefits you. Your story matters.

**As Published:** <https://doi.org/10.1007/s00382-018-4516-5>

**Publisher:** Springer Berlin Heidelberg

**Persistent URL:** <https://hdl.handle.net/1721.1/131556>

**Version:** Author's final manuscript: final author's manuscript post peer review, without publisher's formatting or copy editing

**Terms of Use:** Article is made available in accordance with the publisher's policy and may be subject to US copyright law. Please refer to the publisher's site for terms of use.



1           **A newly developed APCC SCoPS and its prediction of East Asia**  
2                                   **seasonal climate variability**

3  
4  
5  
6  
7           Suryun Ham<sup>1\*</sup>, A-Young Lim<sup>1</sup>, Suchul Kang<sup>2</sup>, Hyein Jeong<sup>3</sup>, and Yeomin Jeong<sup>1</sup>  
8  
9

10  
11  
12                   <sup>1</sup>Climate Services and Research Department, APEC Climate Center, Korea

13                   <sup>2</sup>Ralph M. Parsons Laboratory, Massachusetts Institute of Technology, USA

14                   <sup>3</sup>Fluid Dynamics and Solid Mechanics (T-3), Theoretical Division, Los Alamos National  
15                                   Laboratory, USA  
16  
17  
18  
19

20                                   *(To be submitted Climate Dynamics)*  
21  
22  
23  
24  
25  
26  
27  
28  
29  
30

31                                   January 2018  
32  
33  
34  
35  
36  
37  
38  
39

---

40  
41           \*Corresponding author address:

42           Suryun Ham, Prediction Research Team, Climate Services and Research Department,  
43           APEC Climate Center, Busan, 48058, Korea

44           E-mail: [suryun01@gmail.com](mailto:suryun01@gmail.com)  
45

## Abstract

46

47       The Asia Pacific Economic Cooperation (APEC) Climate Center (APCC) in-  
48 house model (Seamless Coupled Prediction System: SCoPS) has been newly developed  
49 for operational seasonal forecasting. SCoPS has generated ensemble retrospective  
50 forecasts for the period 1982–2013 and real-time forecasts for the period 2014–current.  
51 In this study, the seasonal prediction skill of the SCoPS hindcast ensemble was  
52 validated compared to those of the previous operation model (APEC Climate Center  
53 Community Climate System Model version 3: APCC CCSM3). This study validated the  
54 spatial and temporal prediction skills of hindcast climatology, large-scale features, and  
55 the seasonal climate variability from both systems. A special focus was the fidelity of  
56 the systems to reproduce and forecast phenomena that are closely related to the East  
57 Asian monsoon system. Overall, both CCSM3 and SCoPS exhibit realistic  
58 representations of the basic climate, although systematic biases are found for surface  
59 temperature and precipitation. The averaged temporal anomaly correlation coefficient  
60 for sea surface temperature, 2-m temperature, and precipitation from SCoPS is higher  
61 than those from CCSM3. Notably, SCoPS well captures the northward migrated  
62 rainband related to the East Asian summer monsoon. The SCoPS simulation also shows  
63 useful skill in predicting the wintertime Arctic Oscillation. Consequently, SCoPS is  
64 more skillful than CCSM3 in predicting seasonal climate variability, including the  
65 ENSO and the Arctic Oscillation. Further, it is clear that the seasonal climate forecast  
66 with SCoPS will be useful for simulating the East Asian monsoon system.

---

67 Key words: APCC in-house model, SCoPS, Seasonal prediction, East Asian monsoon

68 **1. Introduction**

69 It has been demonstrated that a fully coupled general circulation model is the  
70 ultimate tool for subseasonal to seasonal climate prediction. Dynamical prediction  
71 systems have been continuously progressed for operational medium-range weather and  
72 seasonal prediction (e.g., Molteni et al. 1996; Kusunoki et al. 2001; Saha et al. 2006,  
73 2014; Arribas et al. 2011; Molteni et al. 2011; MacLachlan et al. 2015; Lee et al. 2014).  
74 These dynamical prediction models in operational centers are almost fully coupled  
75 climate system models that include comprehensive dynamics and physics of the  
76 atmosphere, land surface, ocean, and sea ice interactions. Many studies have  
77 demonstrated the importance of model resolution and atmospheric physics as well as the  
78 model system on various simulated climate variations. For example, Yao et al. (2016)  
79 suggested that coupled model results with higher resolution lead to improved prediction  
80 skill on produced climate variations over the western equatorial Indian Ocean. Ham et al.  
81 (2014) investigated the effects of an improved coupled system on the simulated seasonal  
82 climate over East Asia.

83 For this reason, operational coupled seasonal forecast systems, including the  
84 Climate Forecast System from the National Centers for Environmental Prediction  
85 (NCEP CFS) (Saha et al. 2014), European Centre for Medium-Range Weather Forecasts  
86 (ECMWF), United Kingdom Meteorological Office (UKMO), and Meteo-France  
87 (MacLachlan et al. 2015), as well as many other research groups, are continuously  
88 updating their seasonal prediction systems with improved physics and increased  
89 resolution. The horizontal resolution of the ECMWF Integrated Forecast System has  
90 increased from T159 (System 3; Anderson et al. 2007) to T255 (System 4; Molteni et al.  
91 2011) (from approximately 125 km to 80 km) with model version updating. The UKMO

92 has also increased the atmospheric resolution of the seasonal prediction system to  
93 N216L85 (approximately 60 km) in Global Seasonal Forecasting System version 5  
94 (GloSea5) (MacLachlan et al. 2015).

95 A number of studies mentioned the importance of initialization processes for the  
96 prediction skill in the coupled system. For example, Kug et al. (2010) have developed a  
97 new method that conducting empirical singular vectors for initial perturbation in an  
98 ensemble prediction system. Ham and Rienecker (2012) suggested an improvement in  
99 the El Niño-Southern Oscillation (ENSO) prediction using the ensemble generation  
100 method in their 20-year reforecast simulation. Koster et al. (2010) mentioned that there  
101 is room for improvement in prediction skills for precipitation and surface temperature in  
102 land surface initialization. Recently, the importance of initializations of land surface or  
103 sea ice content is noted at sub-seasonal to seasonal scales. Prodhomme et al. (2016)  
104 showed that realistic initialization of land surface plays a role of improved prediction  
105 skill. Dirkson et al. (2017) suggested that accurate initialization of sea ice thickness can  
106 improve the seasonal prediction skill for Arctic sea ice area and concentration.

107 Since 2007, the Asia-Pacific Economic Cooperation (APEC) Climate Center  
108 (APCC) has issued global temperature and precipitation prediction information for  
109 every following 3–6 month period via the website (<http://www.apcc21.org>). These  
110 deterministic and probabilistic forecasts have been produced by the well-validated  
111 multi-model ensemble (MME) prediction (Min et al. 2014). Since 2012, the APCC has  
112 provided seasonal prediction data as one provider to the MME prediction system using  
113 the Community Climate System Model version 3 (CCSM3) with sea surface  
114 temperature (SST) nudging from the Global Ocean Data Assimilation System (GODAS)  
115 (APCC CCSM3; Jeong et al. 2008). Recently, the prediction skill of CCSM3 has met

116 the limitations of the old version of the model system with low resolution and simple  
117 initialization. To enhance the quality and application of climate forecast information, the  
118 APCC has developed an in-house prediction model with a research group from the  
119 University of Hawaii, USA. The newly developed high-resolution climate prediction  
120 model, termed the Seamless Coupled Prediction System (SCoPS), is a fully coupled  
121 ocean, atmosphere, land, and sea ice component model with coupled atmosphere-ocean  
122 initialization.

123 Since various validations on historical reforecasts (i.e., hindcast) can provide a  
124 useful guideline for understanding its characteristic, it is very important to further  
125 improve the prediction system. In this paper, the newly developed seasonal prediction  
126 model (SCoPS) is described and evaluated alongside previous operation model (APCC  
127 CCSM3) with a basic validation of the prediction system to reproduce the seasonal  
128 climate variability. We also present analysis of the performance of SCoPS for the East  
129 Asian monsoon system. The paper is divided into the following sections: a brief  
130 description of the APCC CCSM3 and SCoPS framework for hindcast experiments is  
131 provided in section 2; section 3 examines hindcast climatology and prediction skills,  
132 which are closely related to the East Asian climate; and section 4 summarizes the results  
133 and provides major conclusions.

134

## 135 **2. Model description**

### 136 *a. APCC CCSM3*

137 CCSM3 has been designed to produce simulations with reasonable fidelity over a  
138 wide range of resolutions and with a variety of atmospheric dynamical frameworks. It is  
139 a community model system for climate simulation, which includes the Community

140 Atmosphere Model version 3 (CAM3; Collins et al. 2004, 2006), the Community Land  
141 Surface Model version 3 (CLM3; Oleson et al. 2004; Dickinson et al. 2006), and the  
142 Community Sea Ice Model version 5 (CSIM5; Briegleb et al. 2004). The ocean  
143 component is based on the Parallel Ocean Program (POP) version 1.4.3 (Smith and  
144 Gent 2002). Based on generally realistic initial conditions, SST-nudging, an empirical  
145 method for data assimilation, is used for initialization in APCC. Further information on  
146 the APCC CCSM3 is given in Collins et al. (2006), Jeong et al. (2008), and Kim et al.  
147 (2017).

148

149 *b. SCoPS*

150 The International Pacific Research Center (IPRC) and University of Hawaii (UH)  
151 modeling group have developed a new coupled atmosphere-ocean model (POEM)  
152 which is based on the POP v2.0 model for the oceanic component, the Ocean-  
153 Atmosphere-Sea Ice-Soil (OASIS v3.0) coupler, and the ECMWF-Hamburg  
154 Atmospheric Model (ECHAM v4.6) as the atmospheric component (Xiang et al. 2012).  
155 Based on the POEM system, SCoPS has been newly developed as a fully coupled  
156 climate model for seamless prediction of weather and climate (APCC project report  
157 2015). SCoPS consists of the ECHAM version 5.3 (Roeckner et al. 2003, Hagemann et  
158 al. 2006) and the Sea Ice Model version 4.1 (Hunk and Lipscomb 2010). The ocean  
159 component is based on the Parallel Ocean Program (POP) version 1.4.3 (Smith and  
160 Gent 2002). Compared with the POEM model (Xiang et al. 2012) as well as the  
161 previous operational model, APCC CCSM3, SCoPS has some distinct improvements: a  
162 newly developed coupled atmosphere-ocean initialization, implanting a sea ice model,  
163 updated model physics and coupler versions, and an increase in the atmosphere and

164 ocean model resolutions.

165       Triangular truncation of the atmosphere component occurs at wavenumber 159  
166 (480 zonal grid and 240 meridional grids in post-processing). A hybrid coordinate  
167 system is used in the vertical direction with top to 10 hPa: a sigma system at the lowest  
168 model level gradually transforms into a pressure system in the lower stratosphere. The  
169 surface temperature is used as a boundary condition to determine the vertical profile  
170 within the five-layer soil model assuming vanishing heat fluxes at the bottom (10-m  
171 depth). The ocean component configuration is 320 (zonal)  $\times$  384 (meridional) grid  
172 points (meridionally about  $0.3^\circ$  in the near equatorial region) and 40 vertical levels. A  
173 solar absorption component based on specified monthly mean surface chlorophyll  
174 concentrations (Ohlmann 2003) is imbedded. The CICE v4.1 model details can be found  
175 in the study by Hunk and Lipscomb (2010). These model components are coupled by an  
176 OASIS3-MCT coupler interface (Larson et al. 2005). Atmosphere, ocean, and ice  
177 models exchange 36 variables including SST, surface fluxes, and ice components daily.

178       High quality climate forecasting relies on and requires improvement of climate  
179 models and use of advanced data assimilation methods that make full use of observation  
180 data. A synthesized atmosphere-ocean initialization scheme has been newly developed  
181 in this system, combining atmospheric 3-dimensional nudging and ocean 3-dimensional  
182 initialization using Ensemble Adjustment Kalman Filter methods (EAKF, Zhang et al.  
183 2007; Anderson 2001). To generate perturbed initial conditions for the ensemble  
184 hindcasts and forecasts, three major steps are taken: 1) generation of model-compatible  
185 data set from analysis datasets; 2) nudging the model-compatible 3-D reanalysis data  
186 into the model; and 3) generation of perturbed ensemble initial conditions.

187



188 *c. Hindcast simulation*

189 Both systems have reproduced reforecast simulations for evaluating and calibrating  
190 the model simulation. APCC CCSM3 seasonal reforecasts have 10 ensemble members  
191 using the time-lagged method for a 1-month lead 6-month forecast. For a first-guess  
192 data of January 1, 1982, the atmosphere model is integrated for the period from 1971 to  
193 1981 (11 years) using GODAS SST (Behringer et al. 1998). Using reproducing fluxes in  
194 an atmospheric simulation, the POP ocean model is executed for the same period. For  
195 the period 1982 to 2013, the initial condition for January 1, 1982 is nudged on day 1, 6,  
196 11, 16, 21, and the last 5 days of every month using the GODAS vertical ocean  
197 temperature. Further details on the APCC CCSM3 reforecast are given in Jeong et al.  
198 (2008).

199 SCoPS has generated ensemble retrospective forecasts for the period 1982–2013  
200 and real-time forecasts for the period 2014–current. Reforecast simulations commenced  
201 at fixed calendar dates — the 1<sup>st</sup> and 5<sup>th</sup> of each month — with 5 ensemble members  
202 perturbed following Gaussian distribution and integrated up to 7 months for a 1-month  
203 lead 6-month forecast. The ensemble initial conditions for January 1, 1982 are from the  
204 results from a 100-year free run SCoPS simulation. The initial data is assimilated every  
205 day from January 2, 1982 to December 31, 2013 using NCEP CFS reanalysis data (Saha  
206 et al. 2010) and World Ocean Database subsurface profile data including mechanical  
207 bathythermograph data (MBT), expendable bathythermograph data (XBT), profiling  
208 float data (PFL), ocean station data (OSD), conductivity-temperature-depth data (CTD),  
209 drifting buoy data (DRB), and Moored buoy data (MRB) (Boyer et al. 2013). In this  
210 system, the observed temperature (T) and salinity (S) are not only used to correct  
211 themselves but also to correct each other since the conservation of the T-S balance has

212 been shown to be an important factor in successful data assimilation (Zhang et al. 2007).  
213 Vertically, only the profile data above 400 m is used since the deeper ocean is not  
214 expected to affect the seasonal forecast skill. Spatially, the observational data from the  
215 band between 50° S–50° N is used. Meanwhile, in real-time seasonal forecasting for the  
216 period 2014–current, the real-time combined ocean vertical profile dataset for  
217 temperature and salinity from the international Argo project is used for ocean  
218 initialization.

219

#### 220 *d. Evaluation*

221 It is very well known that tropical large-scale circulations, such as Hadley, Walker,  
222 and monsoon are the most important driving source of general circulation at low  
223 latitudes, and their interannual variations largely impact climate characteristics in  
224 various regions. Tanaka et al. (2004) attempted to divide the divergent field in the upper  
225 troposphere into represented circulations such as Hadley, Walker, or global monsoon  
226 using the 200-hPa level seasonal velocity potential. They mentioned that the 200-hPa  
227 velocity potential very well represents overall characteristics such as intensity and  
228 variation in tropical circulations because they are each driven by different dynamical  
229 causes. Tanaka et al. (2004) defined the Hadley circulation as the axisymmetric part of  
230 the circulation, which represents the zonal mean field of the velocity potential. The  
231 monsoon circulation is defined as part of the seasonal variation of the deviation field.  
232 For this reason, the seasonal-mean is subtracted from the deviation field to define the  
233 monsoon circulation. More detailed definitions and analysis from field observations can  
234 be found in Tanaka et al. (2004). In this study, global monsoon circulation information  
235 using upper-level velocity potential from reanalysis and predicted results were evaluated

236 following the methodology of Tanaka et al. (2004).

237 For other validations, SST data was obtained from the monthly National Oceanic  
238 and Atmospheric Administration (NOAA) Optimum Interpolation (OI) SST V2  
239 (Reynolds et al. 2002). The air temperature at 2 m (T2m), mean sea level pressure (SLP),  
240 wind vector, and geopotential height data were obtained from the NCEP reanalysis 2  
241 (RA2) and ERA-Interim reanalysis products (Kanamitsu et al. 2002; Dee et al. 2011)  
242 from 1982. The Global Precipitation Climatology Project (GPCP) version 2.1 combined  
243 precipitation dataset (Adler et al. 2003) and Asian Precipitation — Highly-Resolved  
244 Observational Data Integration Towards Evaluation of the Water Resources  
245 (APHRODITE) datasets (Yatagai et al. 2012) were used.

246

### 247 **3. Results**

#### 248 *a. Systematic biases*

249 Figure 1 shows the spatial distribution of 1-month lead 3-month mean forecast  
250 biases of surface temperature, obtained from CCSM3 and SCoPS for the seasons of  
251 June-July-August (JJA) and December-January-February (DJF). CCSM3 and SCoPS  
252 represent the observed temperature patterns generally well in both seasons. However,  
253 the CCSM3 simulation shows slight warm or cold biases over the Eurasia region and  
254 significant warm biases over South America. In the SCoPS simulation, systematic  
255 biases in surface temperature prediction are significant, especially warm biases over  
256 North and South America and cold biases over the Eurasian region. Pattern correlation  
257 coefficients from both models are quite high, around 0.9 for both seasons. These biases  
258 pattern of 1-month lead-time forecast is almost same to those of 4-month lead-time  
259 forecast, although systematic biases get stronger as the lead time increases (not shown).

260 Figure 2 shows the spatial distribution of precipitation biases of model prediction in  
261 JJA and DJF. The GPCP observations show the peaks of the mean precipitation pattern  
262 over the intertropical convergence zone (ITCZ) on the Pacific as well as the western  
263 Pacific, South China Sea, and equatorial Indian Ocean (not shown here). The CCSM3  
264 and SCoPS hindcast climatology generally well captures the observed wet regions,  
265 although there are different notable biases in the two models. In JJA, the predicted  
266 precipitation in CCSM3 tends to be overestimated over the equatorial central Pacific  
267 and parts of the Indian Ocean. Dry biases are also found in the Atlantic ITCZ, western  
268 Pacific, parts of the Indian Ocean, and the northeastern Pacific. Conversely, the SCoPS  
269 simulation generally tends to overestimate precipitation over the central Pacific ITCZ,  
270 the Atlantic ITCZ, and maritime continental regions. Some dry biases are also found in  
271 the central equatorial Pacific. In DJF, the CCSM3 hindcast shows wet biases over the  
272 eastern Pacific, northern central Pacific, and western Indian Ocean, and dry biases are  
273 exhibited over the eastern Indian Ocean. Conversely, the SCoPS simulation shows  
274 overestimated rainfall over the central Pacific ITCZ in the winter Northern Hemisphere.  
275 Pattern correlation coefficients from SCoPS are higher than those from CCSM3  
276 throughout both seasons.

277 To examine seasonal prediction skill, the anomaly temporal correlation coefficient  
278 (TCC) of the sea surface temperature and precipitation between reanalysis data and 1-  
279 month lead hindcast anomalies are calculated for JJA and DJF (Figs. 3 and 4). The TCC  
280 for the sea surface temperature anomaly for each hindcast simulation compared to  
281 NCEP RA2 data are shown in Fig. 3. Generally, the greatest prediction skill for sea  
282 surface temperature is in the tropics, especially in regions related to the ENSO, with the  
283 northern Pacific and equatorial Atlantic also showing high skill in both models. The

284 SCoPS JJA prediction with 1-month lead shows higher prediction skill over the western  
285 Pacific, equatorial Pacific, and Indian Ocean than CCSM3. For DJF prediction, SCoPS  
286 shows higher skill in the northern Pacific and Indian Ocean than CCSM3. Although the  
287 TCC of temperature indicates the greatest skill over the tropical Pacific, it is quite low  
288 in most of the other areas. An impressive feature of SCoPS is that it maintains a higher  
289 TCC skill over the western northern Pacific and Indian Ocean than CCSM3 for both  
290 seasons.

291 Figure 4 shows the TCC of precipitation for JJA and DJF prediction with a 1-month  
292 lead. The prediction skill for precipitation is greater over the tropics than the extra-  
293 tropics and greater over ocean than land as known from other studies (Kim et al. 2012;  
294 Peng et al. 2011). These patterns from the seasonal prediction skill of CCSM3 and  
295 SCoPS are not much different from those of other seasonal prediction systems (e.g.,  
296 Wang et al. 2009; Kim et al. 2012; Lee et al. 2014). In both season predictions, it is  
297 clear that the skill of SCoPS is higher than that of CCSM3 over the Indian Ocean and  
298 northern western Pacific, although some regions have lower skill.

299 Figure 5 shows the seasonal prediction skill as the averaged temporal correlation  
300 coefficient of the sea surface temperature, 2-m temperature, and precipitation anomalies.  
301 TCC is calculated for 1- to 4-month lead 3-month hindcasts (JJA, DJF) globally and for  
302 the East Asian region. The SST prediction skill is higher than the 2-m temperature and  
303 precipitation for JJA and DJF. The results indicate that the prediction skill generally  
304 decreases to the forecast lead time. Also, the prediction skill from SCoPS for all  
305 variables is significantly higher than CCSM3 for the 1-month lead for both seasons and  
306 both regions, although some variables show lower skill for a long lead time. In  
307 particular, the SST prediction skill from SCoPS is about 0.5 for the East Asian region.

308 Climate variability as well as climatology is also important factor to assess the  
309 seasonal prediction skill. Many studies have analyzed the signal to noise (SN) ratio to  
310 assess the predictability of seasonal prediction system with lead-time (Peng et al. 2011;  
311 Peng et al. 2014). Due to the APCC seasonal forecast system is for 3-month or longer  
312 target season, SN ratio for a fixed target season of JJA from CCSM3 and SCoPS with 1  
313 and 4 month lead-time are shown in figures 6 and 7. Here, ‘signal’ indicates standard  
314 deviations of the ensemble mean, and ‘noise’ indicates standard deviations of ensemble  
315 members about ensemble mean. In other words, the SN ratio is computed as the ratio of  
316 variance of ensemble means, and variance of individual forecasts from the ensemble  
317 mean forecast. Larger (small) SN ratio indicates higher (lower) predictability.

318 Shown in Fig. 6 is the SN ratio for SST, precipitation, and 200 hPa geopotential  
319 heights from CCSM3 and SCoPS with 1 month lead-time. For SST, SN ratio from both  
320 systems shows highest in the eastern equatorial tropical Pacific related to the ENSO.  
321 CCSM3 show high SN ratio in high latitude region in southern hemisphere, while  
322 SCoPS show that in northern Pacific, Greenland, as well as Atlantics. For SN ratio for  
323 precipitation prediction with 1-month lead forecast is largest in the tropics and decreases  
324 in the extratropical latitudes for both systems. For 200 hPa geopotential height, the high  
325 SN ratio is also concentration in Tropics for both models, but SCoPS show higher SN  
326 ratio in broaden region than CCSM3. Also, the reason of low SN ratio in extrtropics is  
327 large standard deviation of individual forecasts from the ensemble mean forecast (i.e.,  
328 noise) (not shown). This finding about ‘noise’ in extratropics is consistent with Peng et  
329 al. (2011).

330 SN ratio for atmospheric variables from CCSM3 and SCoPS with 4 month lead-  
331 time is shown in figure 7. Compared to the results with 1 month lead-time in Fig. 6, SN

332 ratio for all variables shows decrease to the lead-time. For structure of SN ratio for SST,  
333 precipitation from CCSM3 and SCoPS are not much differ each other. However, for SN  
334 ratio of 200 hPa geopotential height, SCoPS is still higher than CCSM3 in tropics.  
335 These results indicate that large-scale circulation related to the height from SCoPS is  
336 more reliable than that from CCSM3 with long lead-time, although both systems have  
337 quite big uncertainty in precipitation. Also, SST forecasts from both systems quite well  
338 stay high signal with 4-month lead-time, it is due to the SST characteristic with slowing  
339 vary.

340 It is well known that the ENSO is the main driver of interannual variability in the  
341 tropics. A good representation of it and its teleconnections are very important for good  
342 climate prediction skill. Figure 8 shows the results of a comparison between the lead  
343 time dependence of the SST TCC and RMSE in the Niño 3.4 and Niño 3 regions, with  
344 the OISST observational dataset for hindcasts initialized in May and November. Overall,  
345 the skill of the Niño indices is generally good, although the skill tends to decrease with  
346 lead time. Both SCoPS and CCSM3 exhibit higher skill for the November-initialized  
347 hindcast than the May-initialized hindcast. SCoPS shows slightly higher skill than  
348 CCSM3 until the 5-month lead time over the Niño 3.4 and Niño 3 regions for the  
349 hindcast initialized in November. However, the skill of SCoPS May-initialized hindcast  
350 is not much more different than CCSM3 for both indices. However, the RMSE of the  
351 SST from SCoPS for the Niño 3.4 region in the run initialized in May is worse than that  
352 from CCSM3 (Fig. 8c), due to the fact that there are cold biases in the tropical Pacific in  
353 the SCoPS prediction.

354

355 *b. East Asian summer climate variability*

356 First, the velocity potential and divergent wind at 200 hPa averaged for JJA are  
357 plotted to examine the summer monsoon variability (Figs. 9a, b, c). In the observed  
358 velocity potential distributions (Fig. 9a), a positive peak with a value of nearly  $20 (\times 10^6$   
359  $\text{m}^2 \text{s}^{-1})$  is located northwest of the Philippines in JJA. The minimum is seen over the  
360 southern Atlantic Ocean, with a value of  $-10 (\times 10^6 \text{m}^2 \text{s}^{-1})$ . Hereafter, the velocity  
361 potential “units” of measurement are assumed to be  $10^6 \text{m}^2 \text{s}^{-1}$  for simplicity. A strong  
362 divergent wind related to the Hadley circulation is shown from the northern to southern  
363 Hemisphere. The combined Hadley, Walker, and monsoon circulation shows a strong  
364 convection located in the Philippines. Both 1-month lead hindcast simulations generally  
365 represent the 200-hPa velocity potential pattern well, and the positive and negative  
366 peaks are also captured. However, the SCoPS simulation tends to overestimate its  
367 intensity, while the CCSM3 run shows a weak intensity over the peak regions in  
368 summer (Figs. 9b, c).

369 To extract the monsoon variability, following Tanaka et al. (2004) deviation from  
370 the zonal and annual mean of velocity potential is calculated (Figs. 9d, e, f). In JJA, the  
371 observations show a dominant positive (negative) peak located over East Asia (Pacific  
372 and Atlantic oceans). This is a feature of the Northern Hemisphere summer, which  
373 includes an upper air divergence over East Asia and an upper air convergence over the  
374 Pacific and Atlantic oceans related to the East Asian summer monsoon. A convection  
375 center located near the Philippines in the mean velocity potential field (Fig. 9a) can be  
376 explained by a superposition between one over land associated with the monsoon  
377 circulation (Fig. 9d) and another near the equator associated with the Walker circulation  
378 (not shown). CCSM3 underestimates the upper air divergence over East Asia and splits  
379 the peak into two over the eastern Pacific, while SCoPS results are closer to the



380 observations than those from the CCSM3 hindcast (Fig. 9f). Based on the results, we  
381 conclude that the overestimated mean velocity potential in the SCoPS simulation (Fig.  
382 9c) is due to the enhanced Hadley circulation (not shown), and the underestimated mean  
383 velocity potential in CCSM3 (Fig. 9b) is due to the weak simulated monsoon circulation  
384 (Fig. 9e). Also, it is sure that large-scale circulation features from SCoPS can expect to  
385 more realistic variability related to the monsoon than that from CCSM3.

386 Figure 10 shows the climatological mean precipitation and the 850-hPa zonal wind  
387 over the East Asian region during summer (June–August) in observations (GPCP and  
388 APHRODITE for precipitation; ERA-Interim reanalysis for zonal wind) and hindcasts  
389 from CCSM3 and SCoPS. Note that horizontal resolution of GPCP is  $2.5^\circ \times 2.5^\circ$ , while  
390 that of APHRODITE is  $0.25^\circ \times 0.25^\circ$  with land-only data. In the climatology for JJA,  
391 two major areas of strong precipitation are observed. One is the main precipitation band  
392 related to the ITCZ over the tropics, and the other one is the extending rainband from  
393 southern China to Japan, which is related to the East Asian summer monsoon (EASM)  
394 (Figs. 10a, b). Local monsoon precipitation maxima are in the oceanic convergence  
395 regions over the northeastern Arabian Sea and the Bay of Bengal, and west of the  
396 Philippines.

397 CCSM3 reproduces the features well; however, precipitation over the northwestern  
398 Pacific is underestimated, and precipitation over the Indian Ocean and western  
399 equatorial Pacific tends to be overestimated (Fig. 10c). Related to this, the low-level  
400 monsoon flow pattern is shifted to the precipitation region. The precipitation from  
401 SCoPS shows a slight overestimation. Narrow and strong bands of precipitation are  
402 indicated over the western areas of India, Indochina, and the Philippines in the high-  
403 resolution APHRODITE data. This extremely localized pattern is known to be due to

404 convection generated by narrow mountain areas (Xie et al. 2006; Lee et al. 2013; Ham  
405 et al. 2016). The observed pattern is very well represented in the SCoPS hindcast, due to  
406 its higher horizontal resolution as compared to CCSM3. Moreover, the SCoPS  
407 simulation represents the area over China, Korea, and Japan remarkably well, where the  
408 seasonal prediction captures the zonally elongated rainband associated with the  
409 Changma front (Fig. 10d).

410 Figure 11 shows latitude-time cross sections for the summer precipitation cycle and  
411 850-hPa zonal winds on two longitudes (70–80 °E and 120–130 °E), which are related  
412 to the Indian and East Asian monsoon. Because precipitation from CCSM3 and SCoPS  
413 is usually focused on the 1-month lead 3-month prediction skill in operational seasonal  
414 forecasts, four hindcast datasets from runs initialized in February, May, August, and  
415 November were merged to validate the represented annual cycle of precipitation and  
416 winds. Both hindcasts generally represent the seasonal propagation of precipitation in  
417 the Indian (70–80 °E) and East Asian monsoon regions (120–130 °E), compared to the  
418 GPCP and reanalysis data. For example, the northward rainband related to the Indian  
419 monsoon (April to July) is generally well represented. However, the CCSM3 simulation  
420 exhibits a weaker peak in the northward propagated rainband as well as strong  
421 precipitation over the subtropics and tropics, compared to observations. In the SCoPS  
422 simulation, the peak of the northward precipitation band and the low-level wind are  
423 captured, although slightly overestimated. However, note that the GPCP observation  
424 does not represent orographic heavy rainfall well due to its low resolution. For the East  
425 Asian monsoon region, a split rainband is shown during June to August, with one arm  
426 over South China Sea, related to the ITCZ, and another over the subtropics, which is  
427 related to the Changma front. Both models exhibit the rain peak over the ITCZ well;

428 however, CCSM3 shows exaggerated precipitation over the equatorial rainband, even in  
429 winter. In the SCoPS annual cycle, the two peak rain seasons are represented quite well,  
430 but slightly overestimated. Remarkably, the northward migrated rainband related to the  
431 Changma during May to August is also captured by SCoPS.

432 In Fig. 12, the capability of CCSM3 and SCoPS in simulating the spatial pattern  
433 and interannual variability of the Asian summer monsoon is examined using the  
434 monsoon index developed by Lee et al. (2014). The EASM index is defined as the zonal  
435 wind anomaly at 850 hPa, averaged over the region between 5–10° N and 130–150° E  
436 minus the average over 25–30° N and 110–130° E. The JJA-mean monsoon indices  
437 from the ensemble reforecasts initialized in May were used. The correlation coefficient  
438 of the EASM index between the reanalysis and the SCoPS prediction (0.743) is higher  
439 than the CCSM3 prediction (0.519). Based on the results, SCoPS shows a credible  
440 representation of monsoon circulation for this region, with useful levels of skill for the  
441 East Asian summer monsoon prediction.

442

#### 443 *c. East Asian winter climate variability*

444 The East Asian winter monsoon (EAWM) is the dominant climate feature over East  
445 Asia during the boreal winter. It leads to significant impacts on the weather and climate  
446 over the East Asian regions (Chen et al. 2005; Zhou et al. 2007; Li and Yang 2010;  
447 Jiang et al. 2013). The EAWM consists of subsystems such as the Siberian high,  
448 Aleutian low, East Asian trough, low-level northerly wind, and high-level East Asian jet  
449 stream. It is well known that a strong EAWM is characterized by a strong Siberian high,  
450 intensified East Asian jet stream, a deepened East Asian trough, strong northerly wind  
451 over East Asia, and frequent cold surges (Ding and Sikka 2006; Park et al. 2011; Jiang

452 et al. 2013). Many climate forecast models show reasonable skill in the East Asian  
453 summer monsoon prediction. However, the EAWM prediction skill on climate forecast  
454 systems is still not fully known, although a few studies have examined the predictability  
455 of the EAWM in various climate prediction models (Kim et al. 2012; Jiang et al. 2013).  
456 In this study, the climatological characteristics and interannual variation of the EAWM  
457 were compared with observations and reanalysis data to confirm the seasonal prediction  
458 skills. Also, the prediction skill for the Arctic Oscillation (AO), which is known to be a  
459 dominant feature of winter climate variability in East Asia, was evaluated for the  
460 CCSM3 and SCoPS hindcasts initialized in November.

461 The northern hemisphere winter (DJF) variation in velocity potential for the  
462 climatological mean with 200-hPa divergent winds is shown in Fig. 13. In the observed  
463 distributions, the positive peak shows its full weakness as a value of 12 units and it is  
464 located to the equatorial western Pacific (Fig. 13a). The location of the negative peak is  
465 near western Africa. The center related to the Australian monsoon is located to the north  
466 of Australia. Both hindcast simulations represent the positive and negative peaks of  
467 velocity potential at 200 hPa well (Figs. 13b, c). The SCoPS simulation plots resemble  
468 observations more than the CCSM3 simulation because the divergent wind from  
469 CCSM3 is stronger than that from SCoPS. Also, the pattern correlation of upper-level  
470 velocity potential fields from SCoPS (0.85) is higher than that from CCSM3 (0.57).

471 Following Tanaka et al. (2004), the deviation from the zonal and annual mean of  
472 the velocity potential is calculated for the northern hemisphere winter monsoon  
473 circulation (Figs. 13d, e, f). In the observations, there are negative peaks over East Asia  
474 and positive peaks over the Pacific. A reversal in the pattern between summer and  
475 winter explains the monsoon circulation quite well (See also Figs. 9). The SCoPS

476 simulation captures the observed peaks related to the East Asian winter monsoon feature,  
477 while the CCSM simulation shows a divided peak over the Australia region. Also, the  
478 SCoPS simulation is closer to the observations in terms of intensity than the CCSM3  
479 hindcast. The pattern correlation of monsoon circulation fields from SCoPS (0.88) is  
480 also significantly higher than that from CCSM3 (0.28).

481 In the lower troposphere, the characteristics of the EAWM are the contrast between  
482 the Siberian high and the Aleutian low. These systems lead to strong northwesterlies  
483 over the eastern marginal regions of the Siberian high (Fig. 14a). This monsoon system  
484 is also related to the East Asian trough along the Korea and Japan regions in the middle  
485 troposphere and the maximization of the jet stream over southeastern Japan in the upper  
486 troposphere (Fig. 14d). The CCSM3 and SCoPS hindcasts represent the climatological  
487 features related to the EAWM well (Figs. 14b, c, e, f). However, the CCSM3 hindcast  
488 shows a stronger Siberian high and Aleutian low, stronger cyclonic circulation in the  
489 trough region, and stronger jet stream than observations. The SCoPS hindcast shows  
490 some biases, including a weak Siberian high and Aleutian low; however, the maximum  
491 jet stream in the upper troposphere and the trough in the middle troposphere are better  
492 captured than in CCSM3. In addition, the hindcasts have biases in simulating the  
493 divergent maritime continental winds compared to observations, with easterlies from  
494 CCSM3 and westerlies from SCoPS. The 500-hPa geopotential height in the CCSM3  
495 simulation is higher than observed except for northeastern China, resulting in a weaker  
496 than observed East Asian trough. On the other hand, the SCoPS hindcast shows a lower  
497 geopotential height than observed except along Korea and Japan, resulting in a weaker  
498 than observed trough. SCoPS generally predicts a weaker zonal wind along the westerly  
499 jet stream than observed.

500 To confirm the prediction skill of the models for interannual variation, the  
501 dynamical EAWM index is shown in Fig. 15. This index was proposed by Li and Yang  
502 (2010) to measure the interannual variability of the EAWM and is defined as the  
503 domain-averaged 200-hPa zonal wind shear. Compared to previous indices, this EAWM  
504 index accounts for several factors influencing the monsoon (e.g., the Arctic Oscillation  
505 and ENSO) and better elucidates the physical processes associated with the EAWM (Li  
506 and Yang 2010; Wang and Chen 2010; Wang et al. 2010). SCoPS realistically represent  
507 the observed variation in most years, with a correlation coefficient of 0.459. However,  
508 CCSM3 shows poorer prediction skill than SCoPS, with a correlation coefficient of  
509 0.245.

510 The Arctic Oscillation (AO) is important climate variability with EAWM in East  
511 Asia, especially during boreal winter. Its intensity and variability play a significant role  
512 to surface temperature, precipitation, and large-scale circulation for extratropical region  
513 in northern hemisphere. However, the prediction skill of the AO variation on a seasonal  
514 timescale is still poor in dynamical forecast systems (Johansson 2007; Kim et al. 2012;  
515 MacLachlan et al. 2015). In this study, the represented AO in CCSM3 and SCoPS were  
516 compared with the NCEP reanalysis data. Following the definition of AO by Thompson  
517 and Wallace (1998), the AO index was calculated as the principal component (PC) of  
518 the first empirical orthogonal function (EOF) mode for monthly mean SLP anomalies  
519 during boreal winter (DJF).

520 Figure 16 shows the results of comparison of the PC time series from RA2, CCSM3,  
521 and SCoPS, for hindcast simulations with November initialization. Results from the all  
522 ensemble prediction are indicated in red (SCoPS) and blue (CCSM3) shading areas. To  
523 compare the prediction skill, the ensemble-averaged AO indices from both models and

524 reanalysis were plotted by solid lines. Both PC time series capture the interannual  
525 variation shown in reanalysis data. The anomaly correlation coefficient between the  
526 observed and predicted AO index is 0.58 for SCoPS but only 0.23 for CCSM3.  
527 Especially, the SCoPS simulation captured the variation in strong positive/negative  
528 phase of AO for the recent period of 2009–2012.

529 Figure 17 shows the SLP patterns regressed onto the leading PC from reanalysis  
530 data and both hindcasts. It was used for individual EOF analysis from each model  
531 ensemble member and a composite map of those regression patterns was plotted. The  
532 pattern from RA2 has a dipole structure over the Arctic, northeastern Pacific, and  
533 Atlantic Ocean (Fig. 17a). CCSM3 represents the negative regression pattern over  
534 Arctic well. However, the positive patterns over Pacific and Atlantic Ocean were totally  
535 not captured. Although SCoPS shows a significant weak AO negative pattern over the  
536 Arctic and the center of the positive regression anomaly over the Atlantic Ocean is  
537 parted, the positive center remains over the northeastern Pacific as in the observation.  
538 The reasonable prediction skill of the AO in SCoPS gives an expectation of good  
539 reliability for extratropical winter surface temperature predictions over East Asia.

540

#### 541 **4. Summary and conclusion**

542 In this paper, a new APCC in-house model, namely SCoPS, is introduced. SCoPS is  
543 a state-of-the-art seasonal prediction system based on a fully-coupled climate model,  
544 coupling atmosphere, ocean, and sea ice with integrated atmosphere-ocean initialization  
545 processes. The SCoPS initialized data for 10-member ensembles are assimilated by  
546 NCEP CFS data and several subsurface profile data. The ensemble hindcast runs are  
547 conducted with SCoPS for 32-year runs (1982–2013).

548 This study evaluated the systematic biases of hindcast climatology, large-scale  
549 features, and the basic performance of seasonal forecasting for major climate variability  
550 from CCSM3 and SCoPS. A special focus was placed on the fidelity of the systems to  
551 reproduce and forecast phenomena that are closely related to the East Asian monsoon  
552 system. In particular, to validate the large-scale circulation related to the East Asian  
553 monsoon system, the global divergent field in the upper troposphere was used following  
554 Tanaka et al. (2004).

555 Overall both CCSM3 and SCoPS exhibit realistic representations of the basic  
556 climate state, although systematic biases were found for sea surface temperature, 2-m  
557 temperature, and precipitation. To examine the seasonal prediction skill, the temporal  
558 correlation coefficients of sea surface temperature and precipitation between  
559 observation and the anomalies of each model were also validated for summer and winter.  
560 Generally, the sea surface temperature has its greatest prediction skill in the tropics,  
561 especially in the ENSO region. Both models also exhibit high skill over the northern  
562 Pacific and equatorial Atlantic. SCoPS shows high prediction skill over almost all  
563 regions compared to CCSM3. The averaged temporal anomaly correlation coefficient  
564 for sea surface temperature, 2-m temperature, and precipitation from SCoPS is also  
565 higher than those from CCSM3. However, the RMSE for SST from SCoPS with 1-  
566 month lead for DJF in the Niño 3 and Niño 3.4 regions is worse than that from CCSM3.  
567 This is because there are cold biases over the tropical Pacific in SCoPS.

568 Notably, SCoPS captures the northward migrated rainband related to the East Asian  
569 summer monsoon system. Further, SCoPS shows a higher correlation coefficient  
570 between the observed and predicted monsoon indices than CCSM3 for both summer  
571 and winter seasons. The SCoPS simulation shows useful skill in predicting the Arctic



572 Oscillation. Consequently, SCoPS is more skillful than CCSM3 in predicting the  
573 seasonal climate variability, including the ENSO, East Asian summer and winter  
574 monsoon, and the Arctic Oscillation.

575 Based on these results, the SCoPS seasonal forecast results are provided to the  
576 APCC multi-model ensemble (MME) system as a new APCC operational model, which  
577 is changed from CCSM3 since November 2017. Validation of real-time forecast skill is  
578 an ongoing work-in-progress. Other climate variabilities including ENSO, Indian Niño,  
579 Atlantic Niño, Pacific-North America pattern will be evaluated. Moreover, an  
580 operational subseasonal forecast system is on the drawing board.

581

## 582 **Acknowledgments**

583 This research was supported by the APEC Climate Center. Also, this study was  
584 supported by the Korea Meteorological Administration. We especially thank KMA's  
585 supercomputer management division for providing us with the supercomputer resource  
586 and consulting on technical support. Also, this research is based on APCC Project  
587 (2015), "Development of APCC Seamless Prediction System" by APCC with a research  
588 group of the University of Hawaii, USA. Some of ocean data were collected and made  
589 freely available by the International Argo Program and the national programs that  
590 contribute to it. (<http://www.argo.ucsd.edu>, <http://argo.jcommops.org>). The Argo  
591 Program is part of the Global Ocean Observing System.

592

593

## 594 **References**

595 Adler, R. F., and Coauthors, 2003: The Version 2 Global Precipitation Climatology  
596 Project (GPCP) monthly precipitation analysis (1979-Present). *J. Hydrometeo.*, 4,  
597 1147-1167.

598 APCC Project Report, 2015: Development of APCC Seamless Prediction System. *Final*  
599 *Report (internal report)*, 103pp, APEC Climate Center.

600 Anderson, D., and coauthors, 2007: Development of the ECMWF seasonal forecast  
601 System 3. *ECMWF Technical Memorandum 503*.

602 Anderson, J. L., 2001: An ensemble adjustment Kalman filter for data assimilation.  
603 *Mon. Wea. Rev.*, **129**, 2884-2903.

604 Arribas, A., and Coauthors, 2011: The GloSea4 ensemble prediction system for seasonal  
605 forecasting. *Mon. Wea. Rev.*, **139**, 1891-1910.

606 Bechtold, P., M. Köhler, T. Jung, F. Doblas-Reyes, M. Leutbecher, M. J. Rodwell, F.  
607 Vitart, and G. Balsamo, 2008: Advances in simulating atmospheric variability with  
608 the ECMWF model: From synoptic to decadal time-scales. *Quart. J. Roy. Meteor.*  
609 *Soc.*, **134**, 1337-1351. doi:10.1002/qj.289.

610 Behringer, D., M. Ji, and A. Leetmaa, 1998: An improved coupled model for ENSO  
611 prediction and implications for ocean initialization. Part I: The ocean data  
612 assimilation system, *Mon. Wea. Rev.*, **126**, 1013-1021.

613 Boyer, T.P., and Coauthors, 2013: World Ocean Database 2013, NOAA Atlas NESDIS  
614 72, S. Levitus, Ed., A. Mishonov, Technical Ed.; Silver Spring, MD, 209 pp.,  
615 <http://doi.org/10.7289/V5NZ85MT>

616 Briegleb, B. P., C. M. Bitz, E. C. Hunke, W. H. Lipscomb, M. M. Holland, J. L.  
617 Schramm, and R. E. Moritz, 2004: Scientific description of the sea ice component

618 in the Community Climate System Model, Version Three. *Tech. Rep. NCAR/TN-*  
619 *463+STR*, National Center for Atmospheric Research, Boulder, CO, 78 pp.

620 Chen, W., S. Yang, and R. Huang, 2005: Relationship between stationary planetary  
621 wave activity and the East Asian winter monsoon, *J. Geophys. Res.*, **110**,  
622 doi:10.1029/2004JD005669.

623 Cohen, J., and J. Jones, 2011: A new index for more accurate winter predictions.  
624 *Geophys. Res. Lett.*, **38**, L21701, doi:10.1029/2011GL049626.

625 Collins, W. D., and Coauthors, 2004: Description of the NCAR Community Atmosphere  
626 Model (CAM3). *Tech. Rep. NCAR/TN-464+STR*, National Center for Atmospheric  
627 Research, Boulder, CO, 226pp.

628 -----, and Coauthors, 2006: The formulation and atmospheric simulation of the  
629 Community Atmosphere Model version 3 (CAM3). *J. Climate*, **19**, 2144-2161.

630 Dee, D. P., and Coauthors, 2011: The ERA-Interim reanalysis: configuration and  
631 performance of the data assimilation system. *Quart. J. Roy. Meteor. Soc.*, **137**, 553-  
632 597.

633 Derome, J., H. Lin, and G. Brunet, 2005: Seasonal forecasting with a simple general  
634 circulation model: Predictive skill in the AO and PNA. *J. Climate*, **18**, 597-609,  
635 doi:10.1175/JCLI-3289.1.

636 Dickinson, R. E., K. W. Oleson, G. Bonan, F. Hoffman, P. Thornton, M. Vertenstein, Z.-  
637 L. Yang, and X. Zeng, 2006: The Community Land Model and its climate statistics  
638 as a component of the Community Climate System Model. *J. Climate*, **19**, 2302-  
639 2324.

640 Ding, Y., and D. R. Sikka, 2006: Synoptic systems and wather, in *The Asian Monsoon*,  
641 edited by B. Wang, pp. 141-201, Praxis, New York.

642 Dirkson, A., W. J. Merryfield, A. Monahan, 2017: Impacts of Sea ice thickness  
643 initialization on seasonal arctic sea ice predictions. *J. Climate*, **30**, 1001-1016.

644 Folland, C.K., A. A. Scaife, J. Lindesay, D. B. Stephenson, 2012: How potentially  
645 predictable is northern European winter climate a season ahead? *Int. J. Climatol.*,  
646 **32**, 801-818, doi:10.1002/joc.2314.

647 Hagemann, S., K. Arpe, and E. Roeckner, 2006: Evaluation of the hydrological cycle in  
648 the ECHAM5 model. *J. Climate*, **19**, 3810-3827.

649 Ham, S., S.-Y. Hong, and S. Park, 2014: A study on air-sea interaction on the simulated  
650 seasonal climate in an ocean-atmosphere coupled model. *Clim. Dyn.*, **42**, 1175-  
651 1187.

652 Ham, S., J.-W. Lee, K. Yoshimura, 2016: Assessing future climate changes in the East  
653 Asian summer and winter monsoon using regional spectral model. *J. Meteor. Soc.  
654 Japan*, **94A**, 69-87.

655 Ham, Y.-G., and M. M. Rienecker, 2012: Flow-dependent empirical singular vector with  
656 an ensemble Kalman filter data assimilation for El Niño prediction. *Clim. Dyn.*, **39**,  
657 1727-1738.

658 Hunk, E. C., and W. H. Lipscomb, 2010: CICE: The Los Alamos Sea Ice Model  
659 Documentation and Software User's Manual Version 4.1. LA-CC-06-012, T-3 Fluid  
660 Dynamics Group, Los Alamos National Laboratory, Los Alamos N.M.

661 Hwang, Y.-T., and D. M. W. Frierson, 2013: Link between the double-intertropical  
662 convergence zone problem and cloud biases over the Southern Ocean. *Proc. Natl.  
663 Acad. Sci.*, **110**, 4935-4940.

664 Jeong, H.-I., and Coauthors, 2008: Experimental 6-month hindcast and forecast  
665 simulation using CCSM3. *APCC 2008 Technical Report*, APEC Climate Center.

666 Jiang, X., S. Yang, Y. Li, A. Kumar, W. Wang, and Z. Gao, 2013: Dynamical prediction  
667 of the East Asian winter monsoon by the NCEP Climate Forecast System. *J.*  
668 *Geophys. Res. Atmos.*, **118**, 1312-1328, doi:10.1002/jgrd.50193.

669 Johansson, Å., 2007: Prediction skill of the NAO and PNA from daily to seasonal time  
670 scale. *J. Climate*, **20**, 1957-1975, doi:10.1175/JCLI4072.1.

671 Kanamitsu, M. and Coauthors, 2002: NCEP dynamical seasonal forecast system 2000.  
672 *Bull. Am. Meteor. Soc.*, **83**, 1019-1037.

673 Kim, H.-M., P. J. Webster and J. A. Curry, 2012: Seasonal prediction skill of ECMWF  
674 System 4 and NCEP CFSv2 retrospective forecast for the Northern Hemisphere  
675 Winter. *Clim. Dyn.*, **39**, 2957-2973.

676 Kim, S. T., H.-I. Jeong, and F.-F. Jin, 2017: Mean bias in seasonal forecast model and  
677 ENSO prediction error. *Sci. Rep.*, **7**, doi: 10.1038/s41598-017-05221-3.

678 Koster, R. D., and Coauthors, 2010: Contribution of land surface initialization to  
679 subseasonal forecast skill: First results from a multi-model experiment. *Geophys.*  
680 *Res. Lett.*, **37**, L02402, doi:10.1029/2009GL-041677.

681 Kug, J.-S., Y.-G. Ham, M. Kimoto, F.-F. Jin, and I.-S. Kang, 2010: New approach for  
682 optimal perturbation method in ensemble climate prediction with empirical singular  
683 vector. *Clim. Dyn.*, **35**, 331-340, doi:10.1007/s00382-009-0664-y.

684 Kusunoki, S., M. Sugi, A. Kitoh, C. Kobayashi, K. Takano, 2001: Atmospheric seasonal  
685 predictability experiments by the JMA AGCM. *J. Meteor. Soc. Japan*, **79**, 1183-  
686 1206.

687 Larson, J., R. Jacob, and E. Ong, 2005: The Model Coupling Toolkit: A new fortran90  
688 toolkit for building Multiphysics parallel coupled models. *Int. J. High Perf. Comp.*  
689 *App.*, **19**, 277-292.

690 Lee, J.-W., S.-Y. Hong, E.-C. Chang, M.-S. Suh, and H.-S. Kang, 2013: Assessment of  
691 future climate change over East Asia due to the RCP scenarios downscaled by  
692 GRIMs-RMP. *Clim. Dyn.*, **42**, 733-747.

693 Lee, M.-I., H. S. Kang, D. Dim, D. Kim, H. Kim, and D. Kang, 2014: Validation of the  
694 experimental hindcasts produced by the GloSea4 seasonal prediction system. *Asia-  
695 Pac. J. Atmos. Sci.*, **50(3)**, 307-326.

696 Li, Y., and S. Yang, 2010: A dynamical index for the East Asian winter monsoon, *J.  
697 Climate*, **23**, 4255-4262.

698 Lin, S. and R. B. Rood, 1996: Multidimensional flux-form semi-Lagrangian  
699 transportation schemes. *Mon. Wea. Rev.*, **124**, 2046-2070.

700 MacLachlan, C., and Coauthors, 2015: Global Seasonal forecast system version 5  
701 (GloSea5): a high-resolution seasonal forecast system. *Quart. J. Roy. Meteor. Soc.*,  
702 **141**, 1072-1084. doi:10.1002/qj.2396.

703 Min, Y.-M., V. N. Kryjov, and S. M. Oh, 2014: Assessment of APCC multimodel  
704 ensemble prediction in seasonal climate forecasting: Retrospective (1983–2003)  
705 and real-time forecasts (2008–2013), *J. Geophys. Res. Atmos.*, **119**, 12,132–12,150,  
706 doi:10.1002/2014JD022230.

707 Molteni, F., R. Buizza, T. N. Palmer, and T. Petroligis, 1996: The ECMWF ensemble  
708 prediction system: Methodology and validation. *Quart. J. Roy. Meteor. Soc.*, **122**,  
709 73-119. doi: 10.1002/qj.49712252905.

710 Molteni, F., and coauthors, 2011: The new ECMWF seasonal forecast system (System  
711 4). ECMWF Technical Memorandum No. 656.

712 Ohlmann, J. C., 2003: Ocean radiant heating in climate models. *J. Climate*, **16**, 1337-  
713 1351.

714 Oleson, K. W., and Coauthors, 2004: Technical description of the Community Land  
715 Model (CLM). *Tech. Rep. NCAR/TN-461+STR*, National Center for Atmospheric  
716 Research, Boulder, CO, 174pp.

717 Park, T.-W., C.-H. Ho, S. Yang, 2011: Relationship between the Arctic Oscillation and  
718 cold surges over East Asia. *J. Climate*, **24**, 68-83.

719 Peng, P., A. Kumar, W. Wang, 2011: An analysis of seasonal predictability in coupled  
720 model forecasts. *Clim. Dyn.*, **36**, 419-430.

721 Peng, P., A. Kuma, B. Jha, 2014: Climate mean, variability and dominant patterns of the  
722 Northern Hemisphere winter mean atmospheric circulation in the NCEP CFSv2.  
723 *Clim. Dyn.*, **42**, 2783-2799.

724 Prodhomme, C., F. Doblas-Reyes, O. Bellprat, E. Dutra, 2016: Impact of land-surface  
725 initialization on sub-seasonal to seasonal forecasts over Europe. *Clim. Dyn.*, **47**,  
726 919-935.

727 Reynolds, R. W., N.A. Rayner, T.M. Smith, D.C. Stokes, and W. Wang, 2002: An  
728 improved in situ and satellite SST analysis for climate. *J. Climate*, **15**, 1609-1625.  
729 [NOAA\_OI\_SST\_V2 data provided by the NOAA/OAR/ESRL PSD, Boulder,  
730 Colorado, USA, from their Web site at <http://www.esrl.noaa.gov/psd/> ]

731 Roeckner, E., G. Buml, L. Bonaventura, and Coauthors, 2003: The atmospheric general  
732 circulation model ECHAM5. Part I: Model description. MPI Reprot 349, Max  
733 Planck Institute for Meteorology, Hamburg, Germany, 127pp.

734 Saha, S., and Coauthors, 2006: The NCEP climate forecast system. *J. Climate*, **19**,  
735 3483-3517.

736 -----, and Coauthors, 2010: The NCEP climate forecast system reanalysis.  
737 *Bulletin of the American Meteorological Society*, **91**, 1015-1057,  
738 doi:10.1175/2010BAMS3001.1

739 -----, and Coauthors, 2014: The NCEP climate forecast system version 2. *J.*  
740 *Climate*, **27**, 2185-2208.

741 Smith, R. D., and P. R. Gent, 2002: Reference manual for the Parallel Ocean Program  
742 (POP), ocean component of the Community Climate System Model (CCSM2.0 and  
743 3.0). Tech. Rep. LA-UR-02-2484, Los Alamos National Laboratory. [Available  
744 online at <http://www.cesm.ucar.edu/models/ccsm3.0/pop.>]

745 Tanaka, H. L., N. Ishizaki and A. Kitoh, 2004: Trend and interannual variability of  
746 Walker, monsoon and Hadley circulations defined by velocity potential in the upper  
747 troposphere, *Tellus*, **56A**, 250-269.

748 Thompson, D. W. J., and J. M. Wallace, 1998: The Arctic Oscillation signature in the  
749 wintertime geopotential height and temperature fields. *Geophys. Res. Lett.*, **25**,  
750 1297-1300, doi:10.1029/98GL00950.

751 Wang, B., and Coauthors, 2009: Advance and prospectus of seasonal prediction:  
752 assessment of the APCC/CliPAS 14-model ensemble retrospective seasonal  
753 prediction (1980-2004). *Clim. Dyn.*, **33**, 93-117, doi:10.1007/s00382-008-0460-0.

754 Wang, L., and W. Chen, 2010: How well do existing indices measure the strength of the  
755 East Asian winter monsoon? *Adv. Atmos. Sci.*, **27**, 855-870.

756 -----, W. Chen, W. Zhou and Coauthors, 2010: Effect of the climate shift around  
757 mid 1970s on the relationship between wintertime Ural blocking circulation and  
758 East Asian climate, *Int. J. Climatol.*, **30**, 153-158.



759 Xiang, B., B. Wang, Q. Ding, F.-F. Jin, and Coauthors, 2012: Reduction of the  
760 thermocline feedback associated with mean SST bias in ENSO simulation. *Clim.*  
761 *Dyn.*, **39**, 1413-1430.

762 Xie, S.-P., H. Xu, N.H. Saji, Y. Wang, and W. T. Liu, 2006: Role of narrow mountains in  
763 large-scale organization of Asian monsoon convection. *J. Climate*, **19**, 3420-3429.

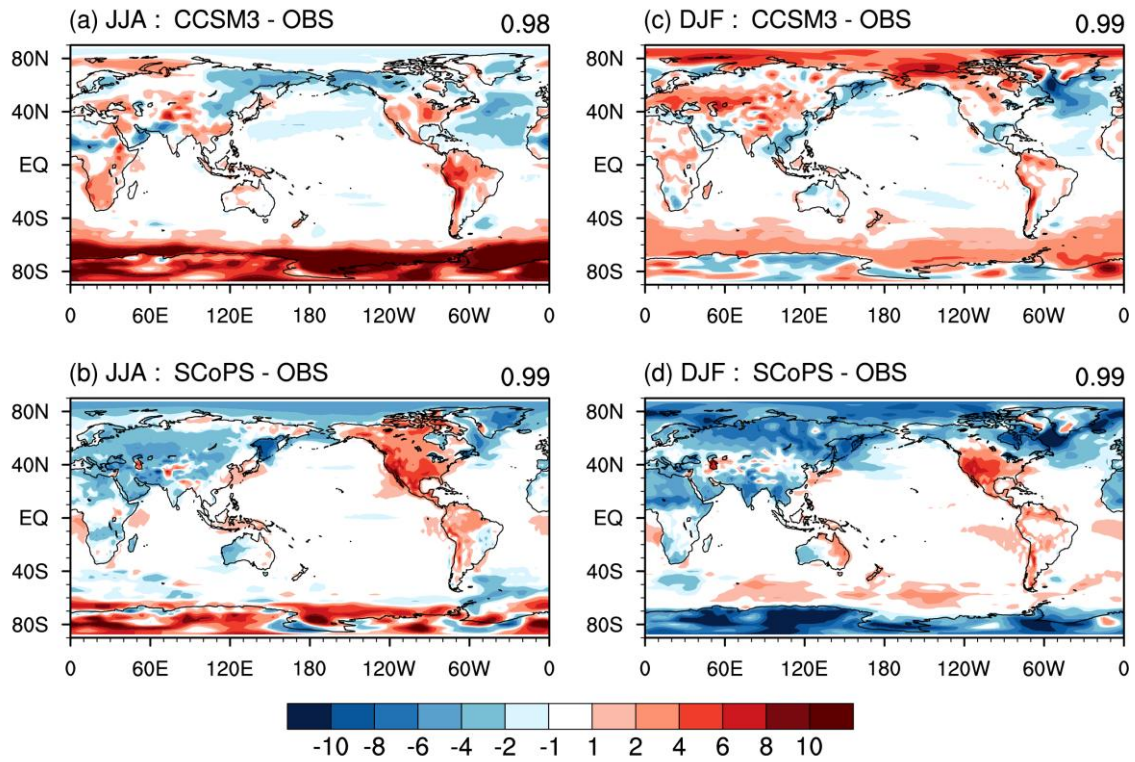
764 Yatagai, A., K. Kamiguchi, O. Arakawa, A. Hamada, N. Yasutomi, and A. Kito, 2012:  
765 APHRODITE: Constructing a long-term daily gridded precipitation dataset for Asia  
766 based on a dense network of rain gauges. *Bull. Amer. Meteor. Soc.*, **93**, 1401-1415.

767 Zhang, G. J., and H. Wang, 2006: Toward mitigating the double ITCZ problem in  
768 NCAR CCSM3. *Geophys. Res. Lett.*, **33**, L06709, doi:10.1029/2005GL025229.

769 Zhang, S., M. J. Harrison, A. Rosati, and A. Wittenberg, 2007: System design and  
770 evaluation of coupled ensemble data assimilation for global oceanic climate studies.  
771 *Mon. Wea. Rev.*, **135**, 3541-3564.

772 Zhou, W., C. Li, and X. Wang, 2007: Possible connection between Pacific Oceanic  
773 interdecadal pathway and East Asian winter monsoon, *Geophys. Res. Lett.*, **34**,  
774 L01701.

775



777

778

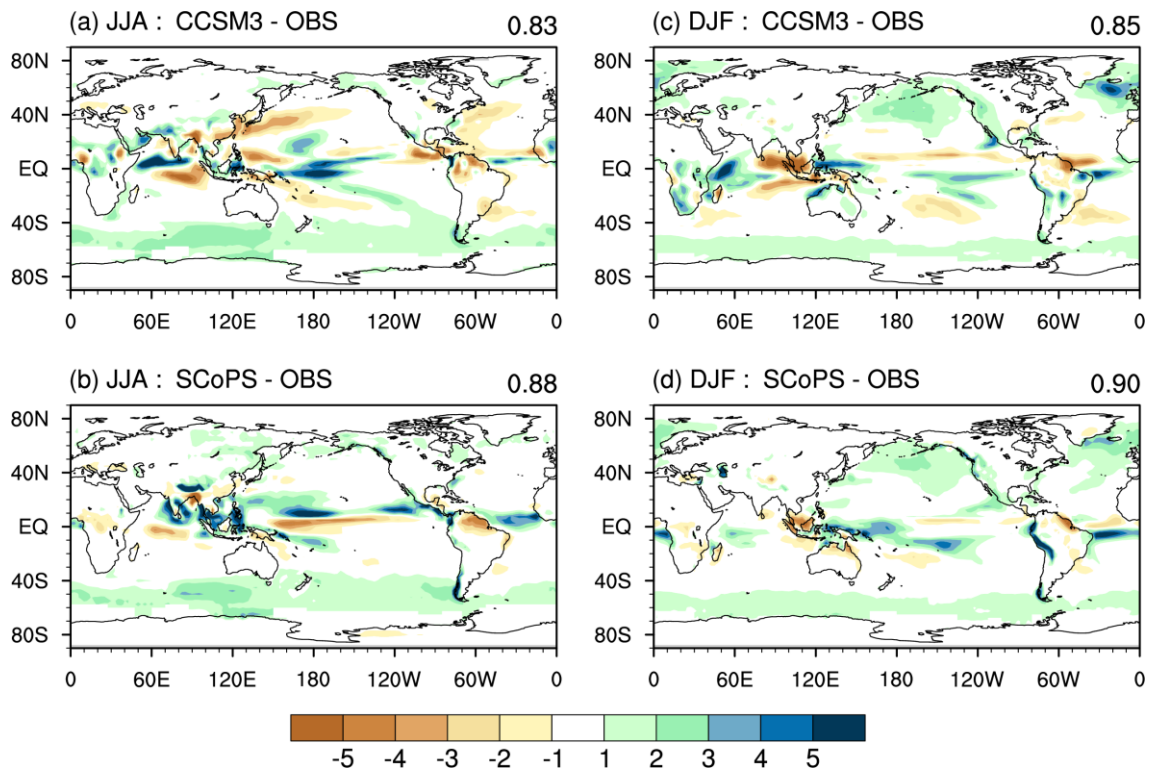
779

780 **Fig. 1.** Spatial distribution of climatological summer (left) and winter (right)  
 781 of the surface temperature biases (model minus observation) for (a), (c)  
 782 CCSM3 and (b), (d) SCoPS. Top-right value indicates the pattern correlation  
 783 coefficient between observation and each prediction.

784

785

786

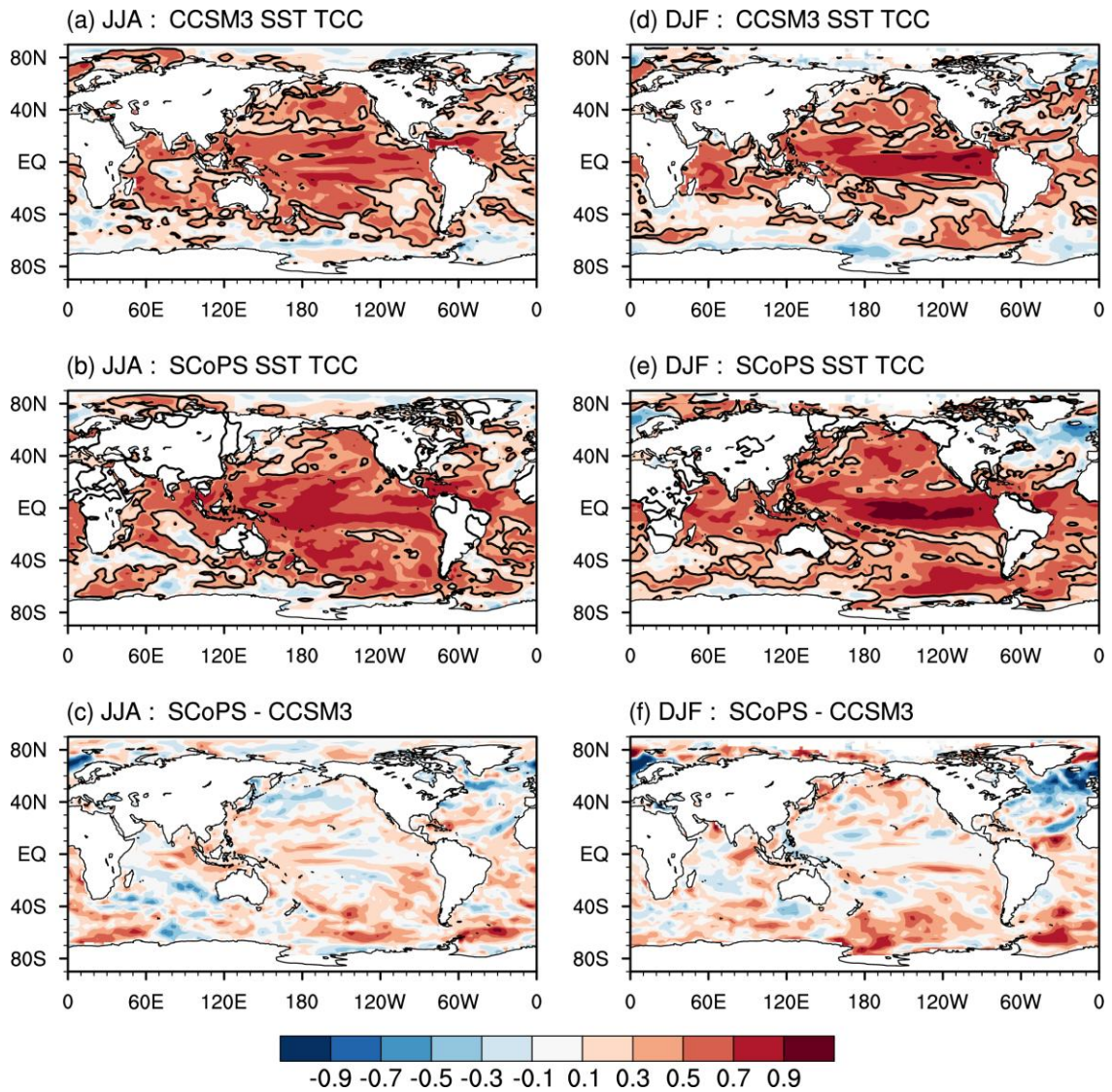


787

788

789 **Fig. 2.** Same as Fig. 1, but for precipitation.

790

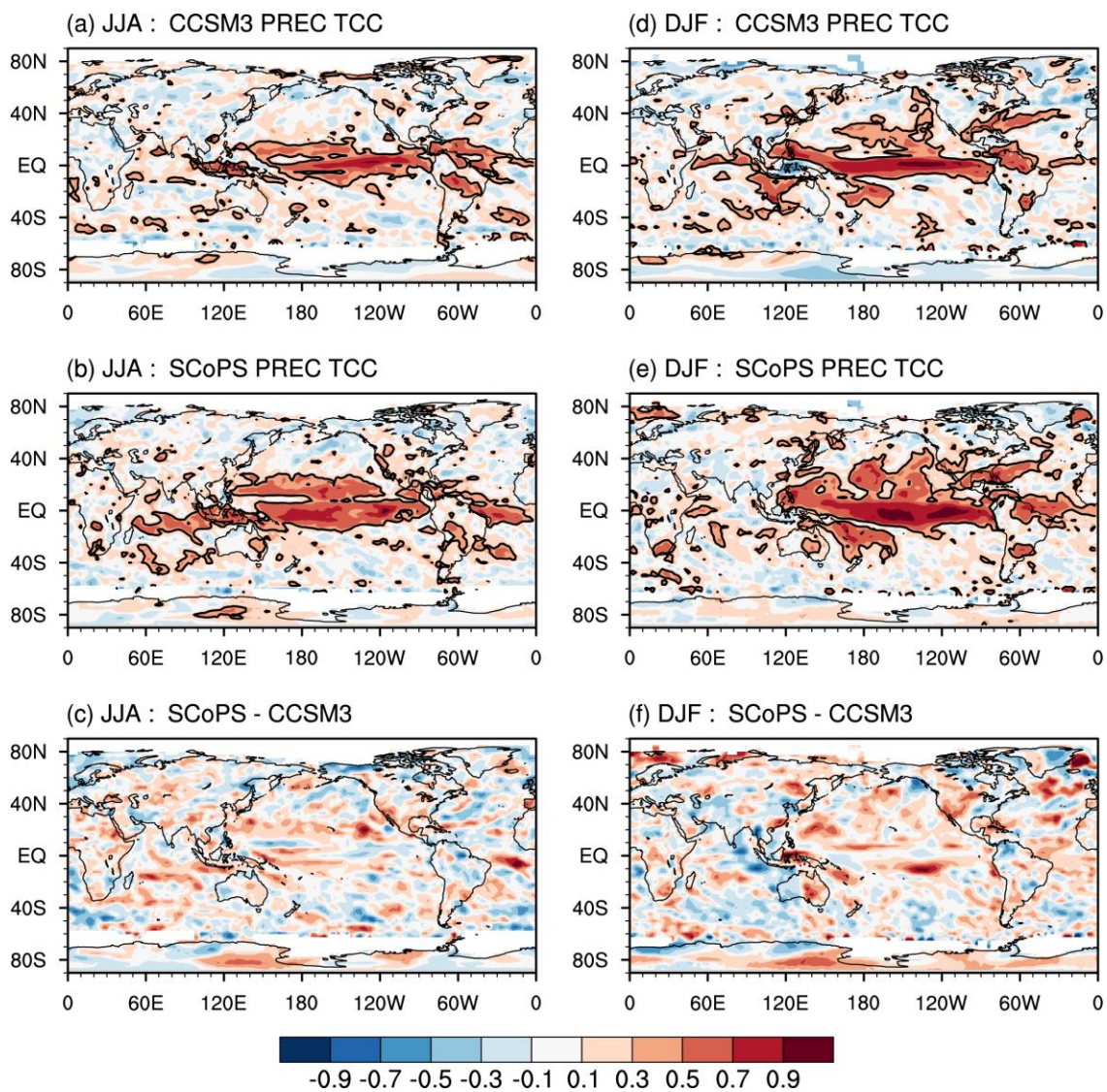


791

792 **Fig. 3.** Prediction skill of the sea surface temperature between observation  
793 and (a) CCSM3 for JJA and (b) SCoPS hindcast with 1-month lead 3-month  
794 mean hindcast for JJA. (c) The difference between (a) and (b). Prediction  
795 skill of the sea surface temperature between observation and (d) CCSM3 for  
796 DJF and (e) SCoPS hindcast with 1-month lead 3-month mean hindcast for  
797 DJF. (f) The difference between (d) and (e). Black thick lines in (a) to (e)  
798 indicates the area statistically significant at the 95% level.

799

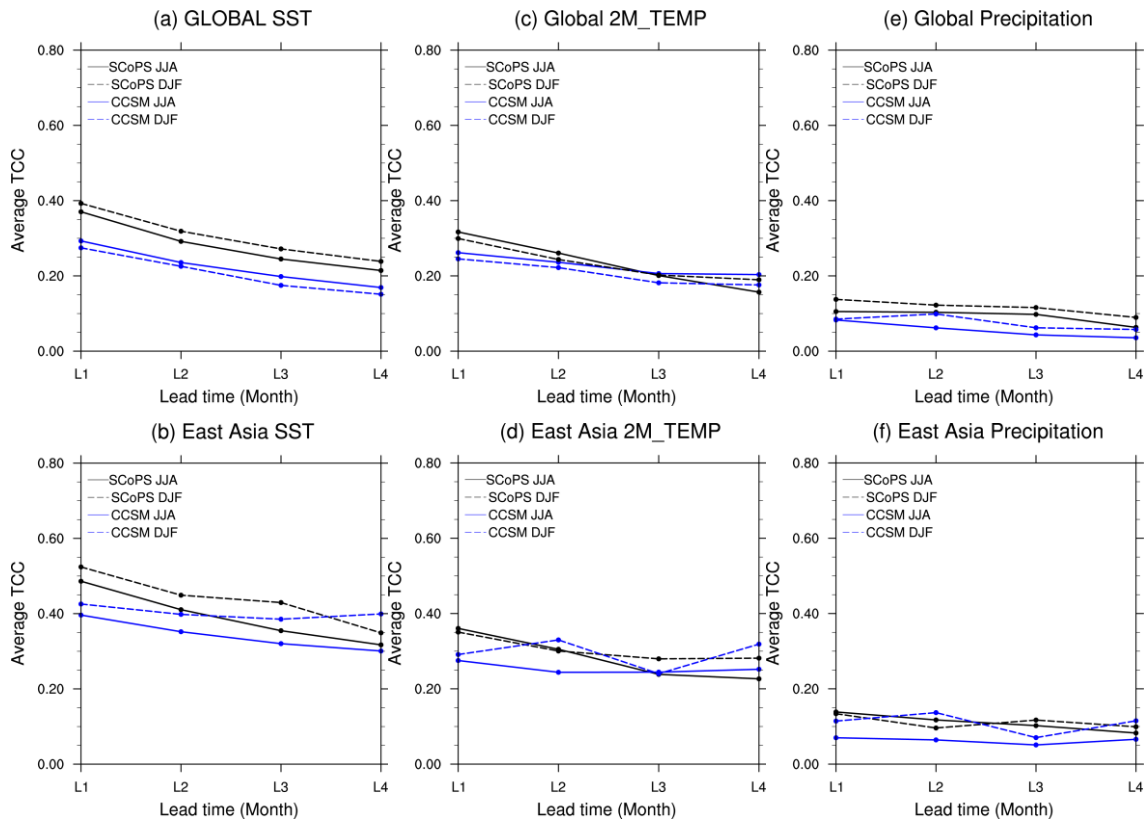
800



801

802 **Fig. 4.** Same as Fig. 3, but for precipitation.

803



804

805

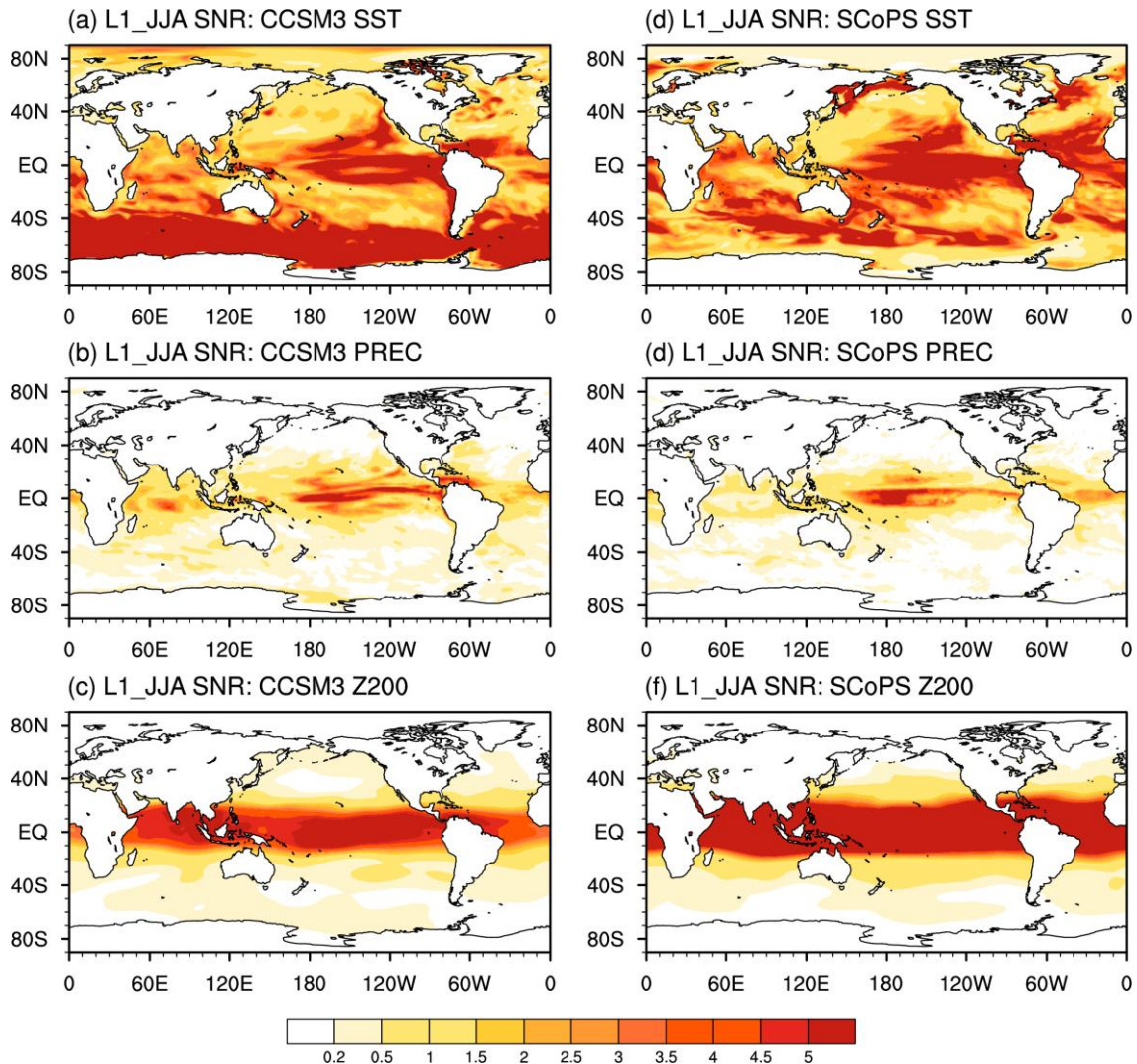
806

807 **Fig. 5.** Averaged TCC (a) for global SST, (b) East Asia SST, (c) global 2-m  
 808 temperature, (d) East Asia 2-m temperature, (e) global precipitation, and (f)  
 809 East Asia precipitation from CCSM3 (blue) and SCoPS (black) with 3-  
 810 month mean hindcast for JJA and DJF.

811

812

813



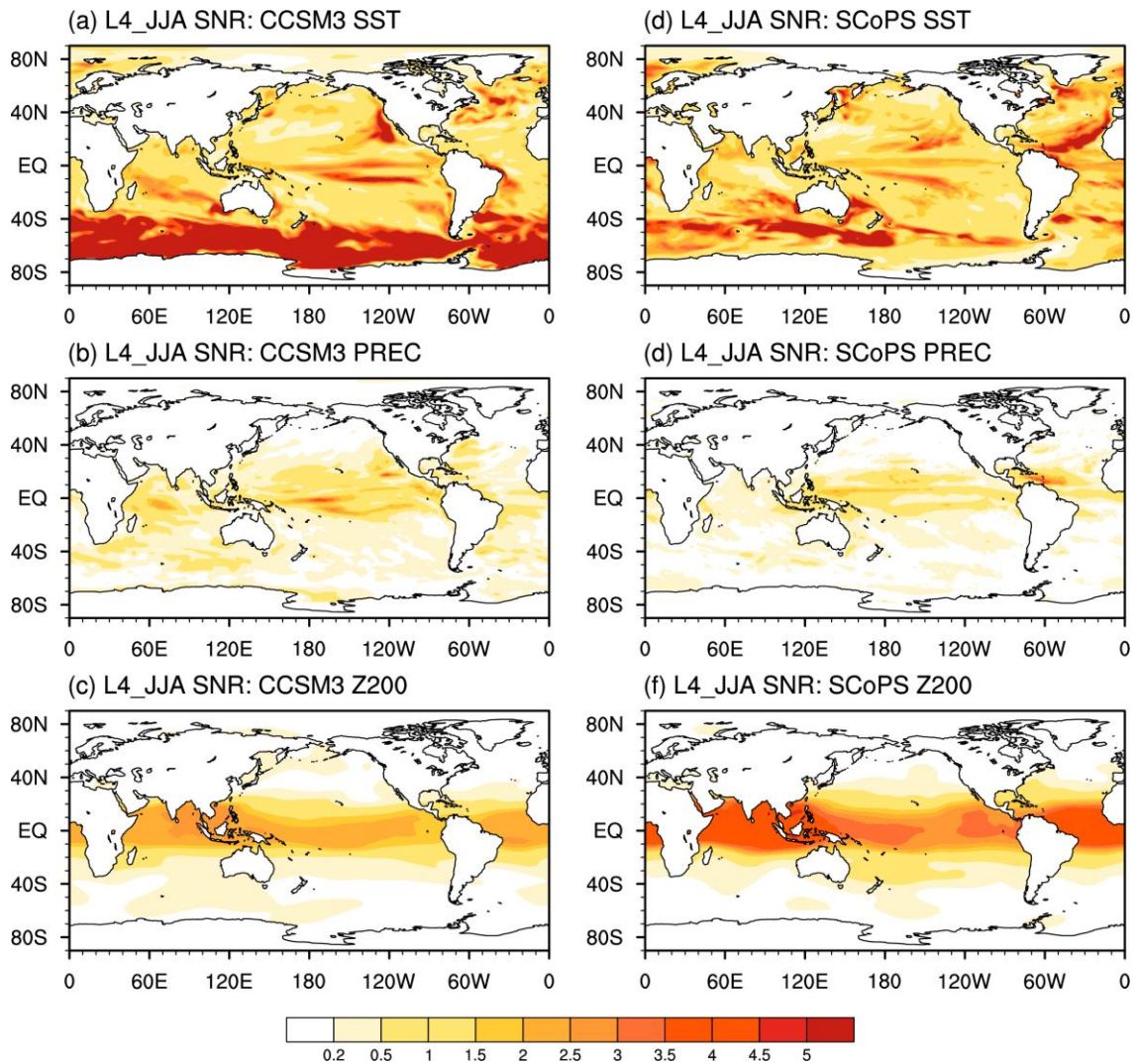
814

815

816 **Fig. 6.** Signal-to-Noise (SN) ratio for (a), (d) SSTs, (b), (d) rainfall, and (c),  
817 (f) 200 hPa geopotential heights from CCSM3 and SCoPS for 1-month lead  
818 time. The SN ratio is computed as the ratio of standard deviation of  
819 ensemble means, and standard deviation of individual forecasts from the  
820 ensemble mean forecast. Larger (small) SN ratio is indicative of higher  
821 (lower) predictability.

822

823



824

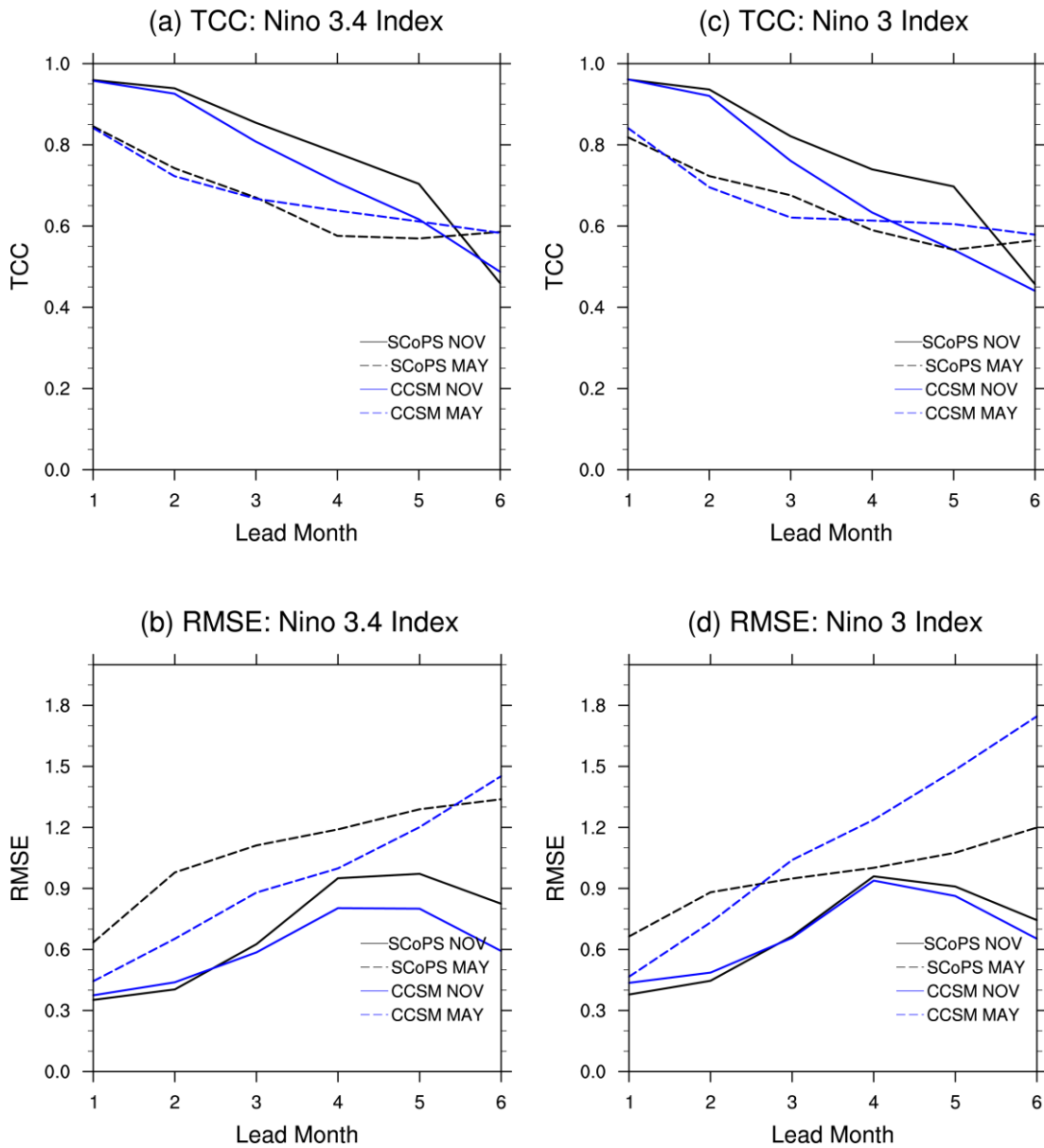
825

826 **Fig. 7.** Same as Fig. 6, but for 4-month lead time.

827



828



829

830

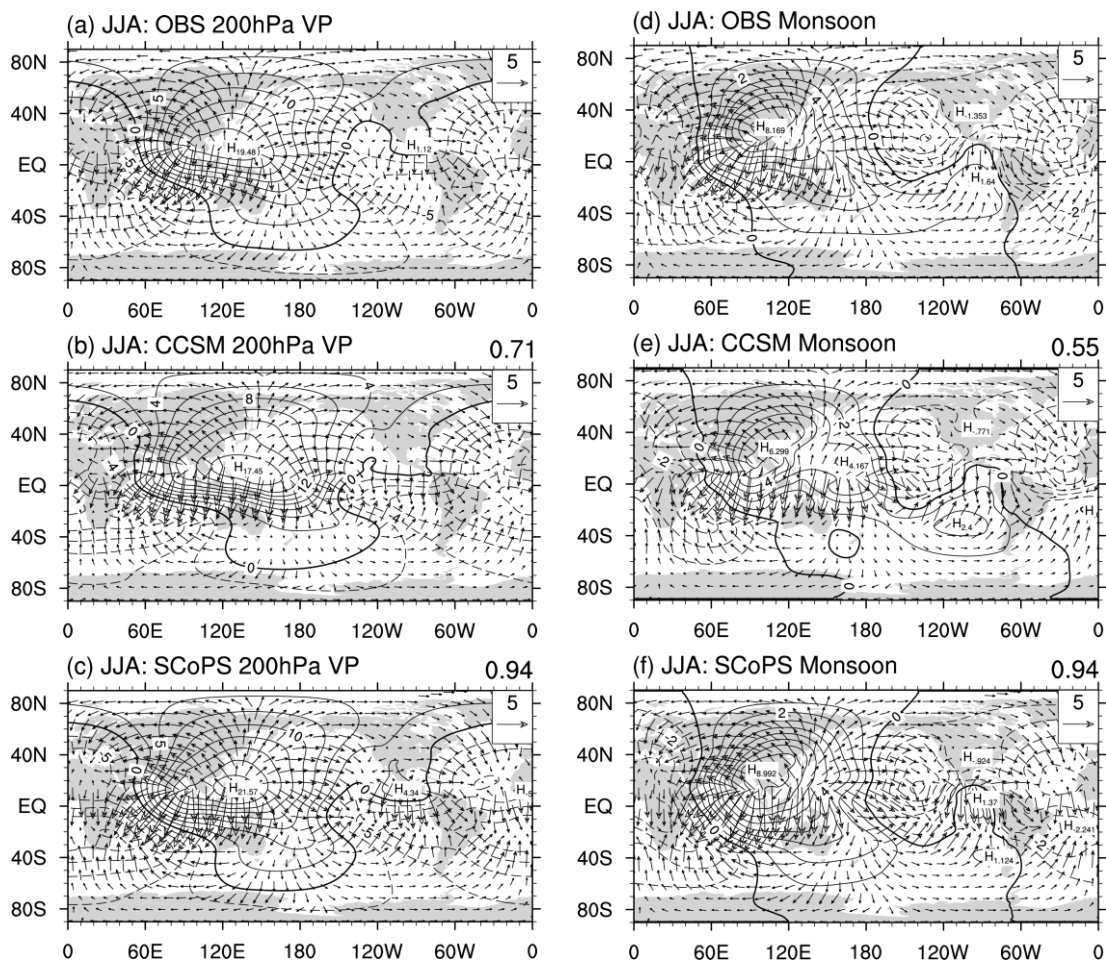
831

832

833 **Fig. 8.** (a) Temporal correlation coefficient of Niño 3.4 indices, (b) root mean  
834 square error of Niño 3.4 indices, (c) temporal correlation coefficient of Niño 3  
835 indices, and (d) root mean square error of Niño 3 indices from CCSM3 (blue),  
836 SCoPS with May-initialized hindcast (black dashed lines), and SCoPS with  
837 November-initialized (black solid lines) hindcast.

838

839  
840



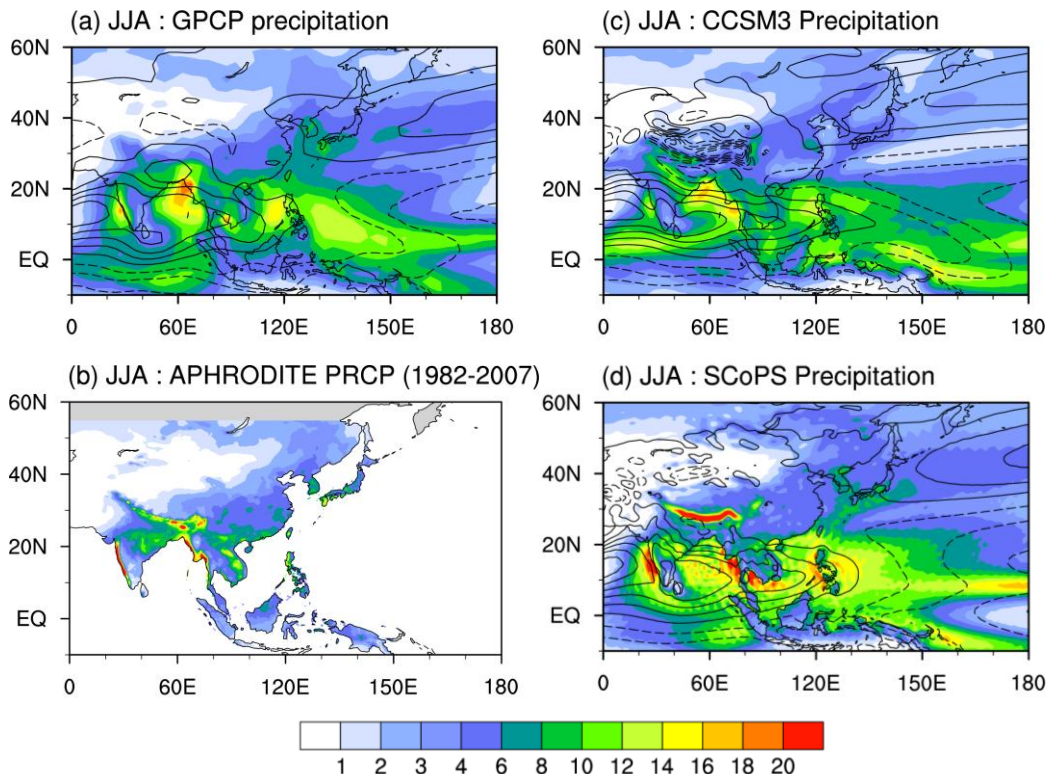
841

842

843 **Fig. 9.** Seasonal mean velocity potential and divergent wind at 200 hPa for  
844 the (a) reanalysis data, (b) CCSM3, and (c) SCoPS hindcast period (1982–  
845 2013) with 1-month lead time for JJA. The monsoon circulations, which are  
846 defined by the seasonal variation of the velocity potential are plotted with  
847 divergent wind for the (d) reanalysis data, (e) CCSM3, and (f) SCoPS  
848 hindcast. The units are  $10^6 \text{ m}^2 \text{ s}^{-1}$ .

849

850

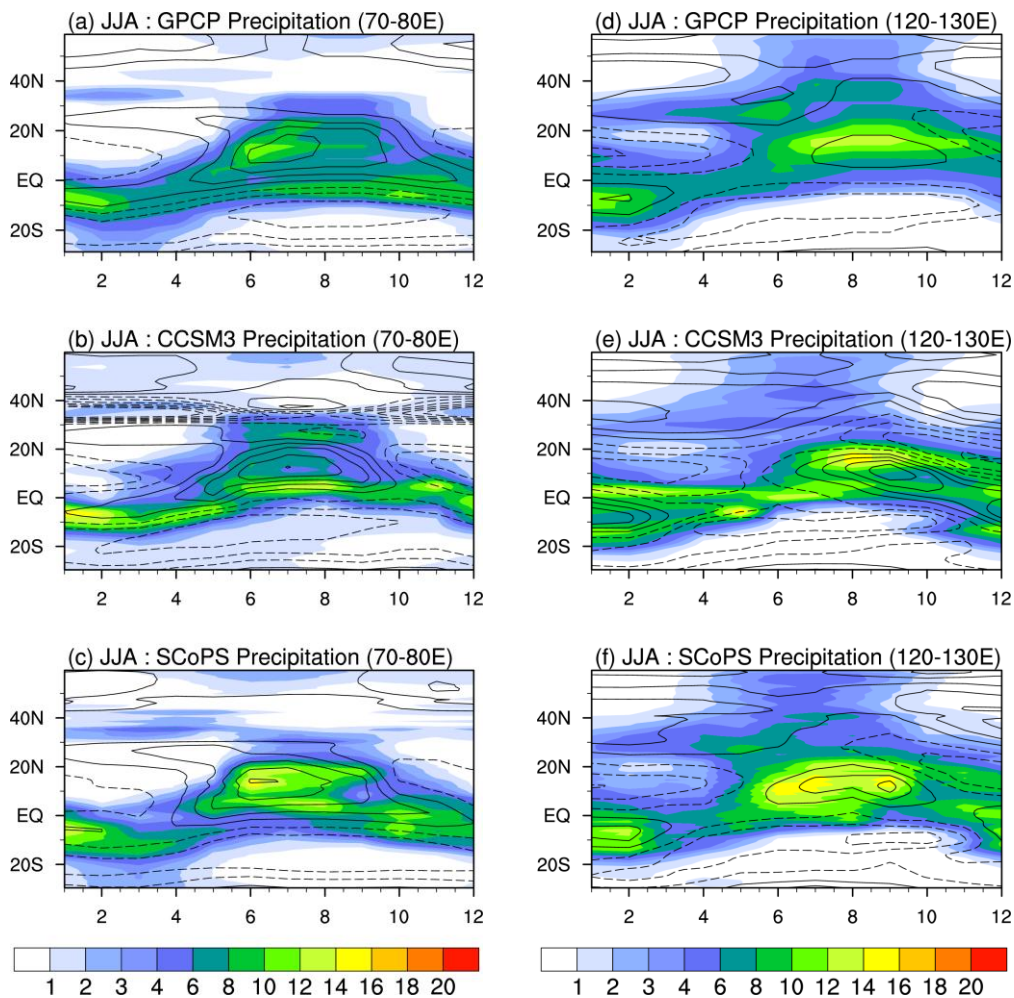


851

852

853 **Fig. 10.** Climatological mean precipitation (shaded) and zonal wind at 850  
 854 hPa (contour) from (a) GPCP and ERA-interim, (b) APHRODITE  
 855 precipitation, (c) CCSM3, and (d) SCoPS during June to August, averaged  
 856 over 32 years (1982–2013). Initial month for both hindcasts is May (1-  
 857 month lead time).

858



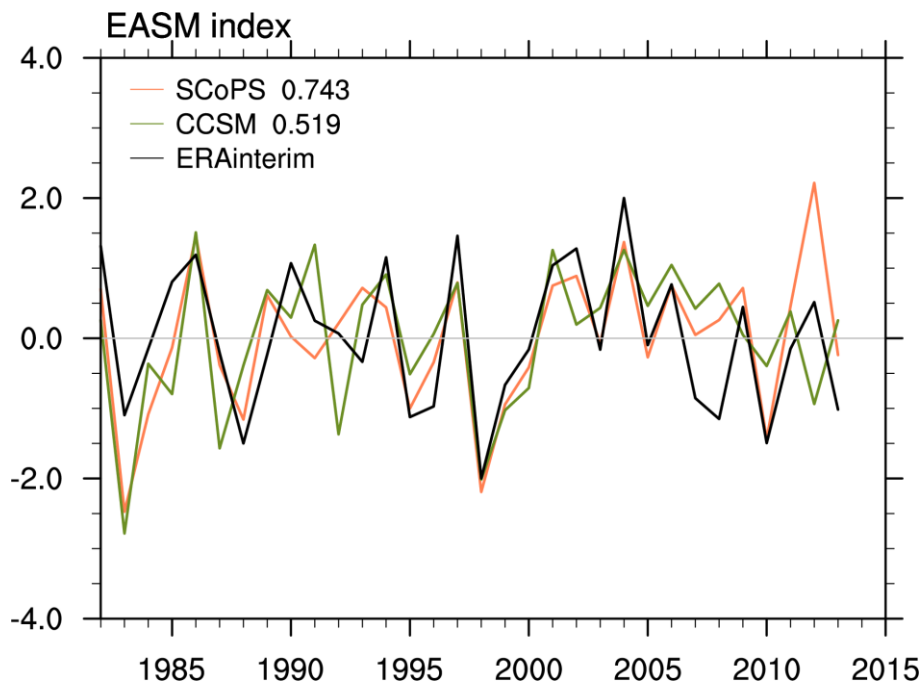
860

861

862 **Fig. 11.** Latitude-time cross section of climatological mean precipitation and  
 863 850-hPa zonal wind from (a) GPCP and ERA-interim over the Indian region  
 864 (70–80 E°), (b) CCSM3 over the Indian region, (c) SCoPS over the Indian  
 865 region, (d) GPCP and ERA-interim over the East Asian region (120–130 E°),  
 866 (e) CCSM3 over the East Asian region, and (f) SCoPS over the East Asian  
 867 region.

868

869



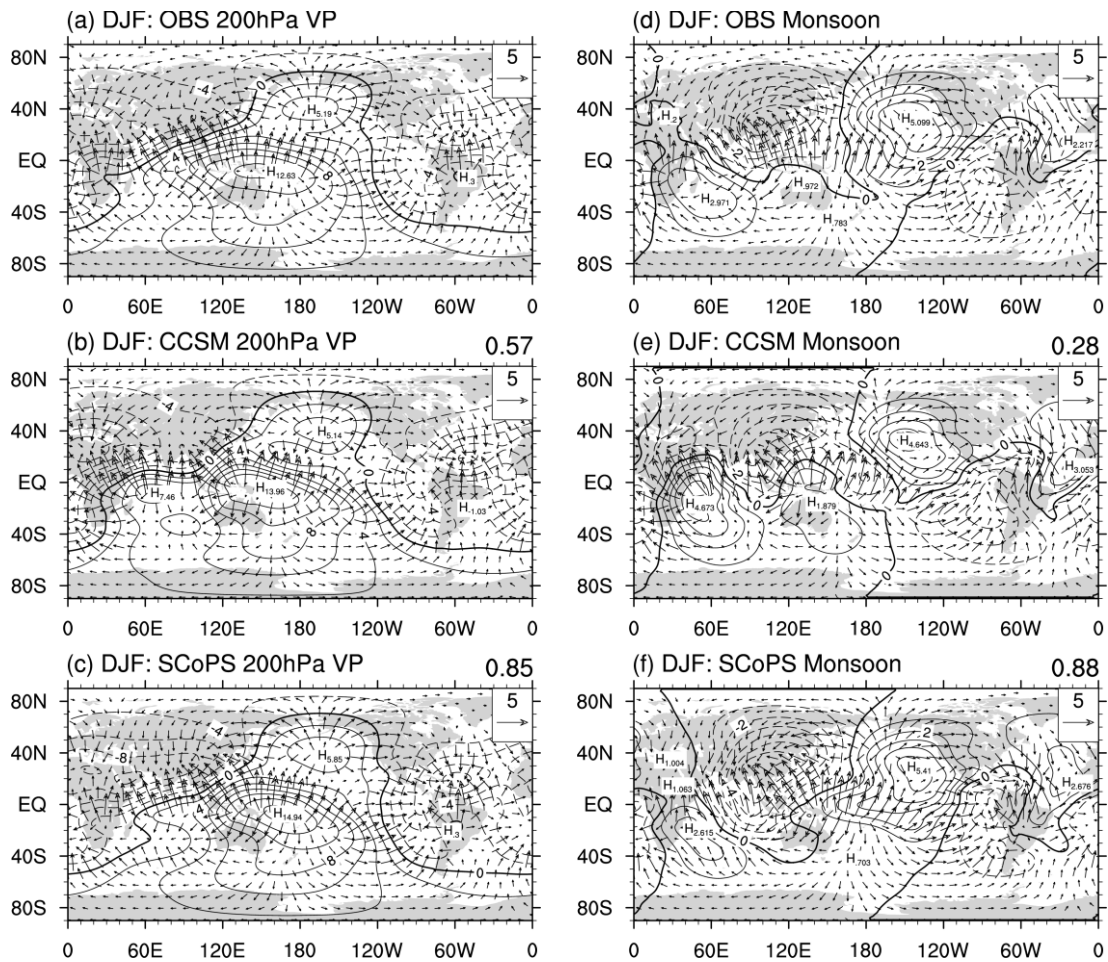
870

871

872

873 **Fig. 12.** The summer (JJA) EASM (East Asian Summer Monsoon) indices  
874 with correlation coefficients from reanalysis data, CCSM3, and SCoPS  
875 hindcasts. EASM is defined as the zonal wind anomaly at 850 hPa, averaged  
876 over the region of 5–10 °N and 130–150 °E minus that over 25–30 °N and  
877 110–130 °E by Lee et al. (2014).

878



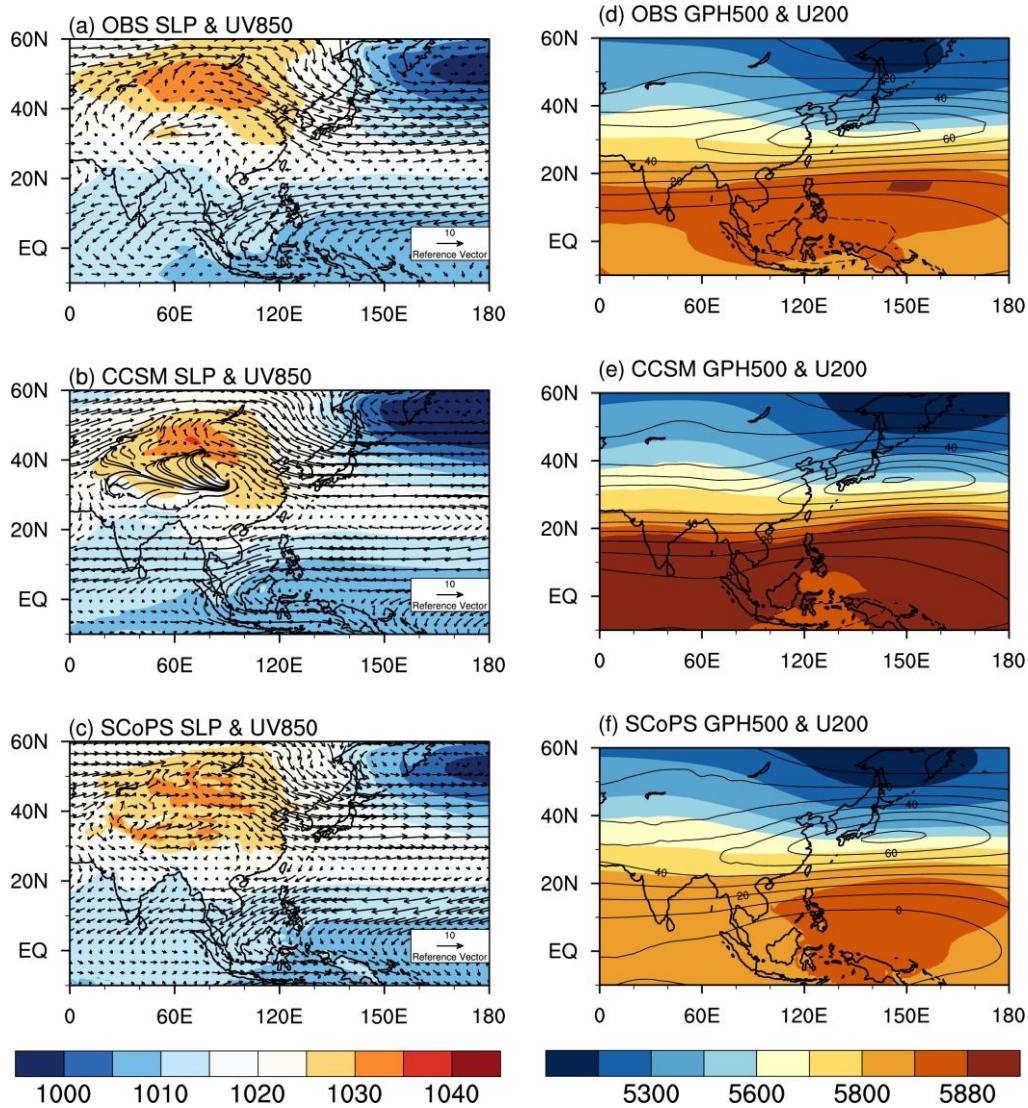
880

881

882 **Fig. 13.** Same as Fig. 9, but for hindcast with starting November.

883

884



886

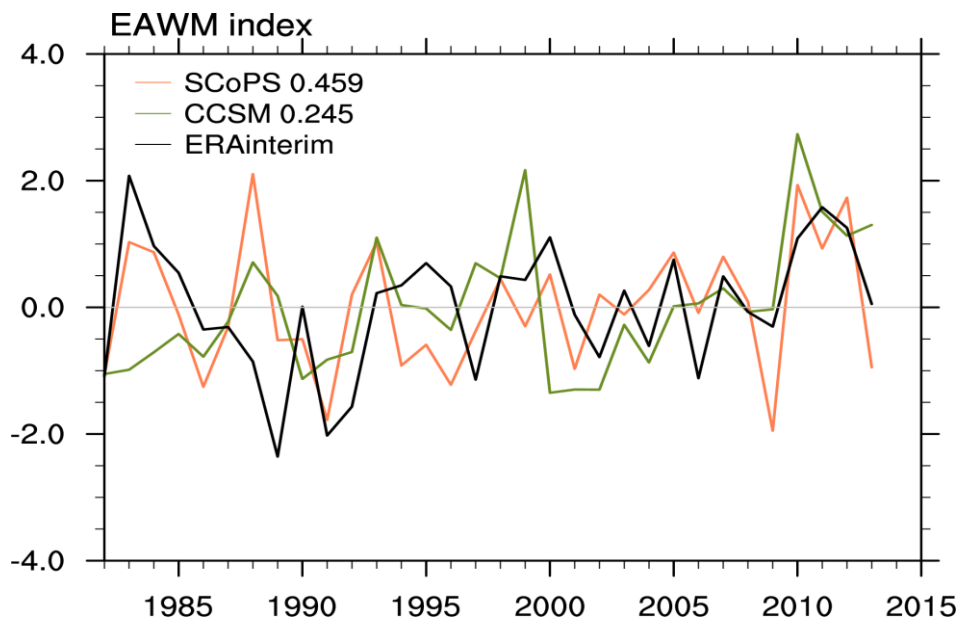
887

888 **Fig. 14.** Climatological mean sea level pressure (left; shaded), wind vector  
 889 at 850 hPa (left; contour), geopotential height (right; shaded), and zonal  
 890 wind at 200 hPa (right; contour) from reanalysis data (top), CCSM3  
 891 (middle), and SCoPS (bottom) during December to February, averaged over  
 892 32 years (1982–2013). Initial month for both hindcasts is November (1-  
 893 month lead time).

894

895

896



897

898

899

900 **Fig. 15.** Normalized EAWM indices from reanalysis (black), CCSM3 (olive),  
901 SCoPS (coral). EAWM is defined as the index from Li and Yang (2010).

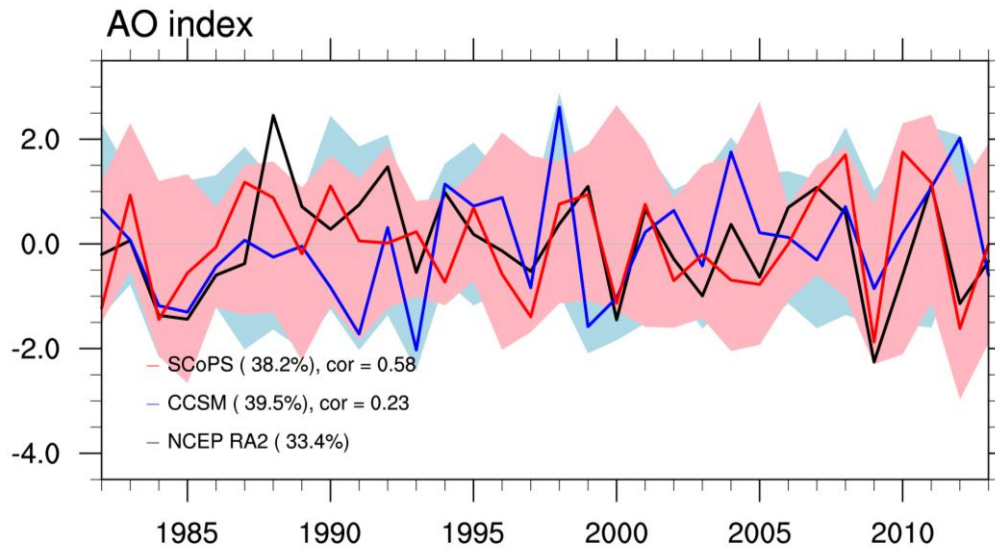
902

903



904

905

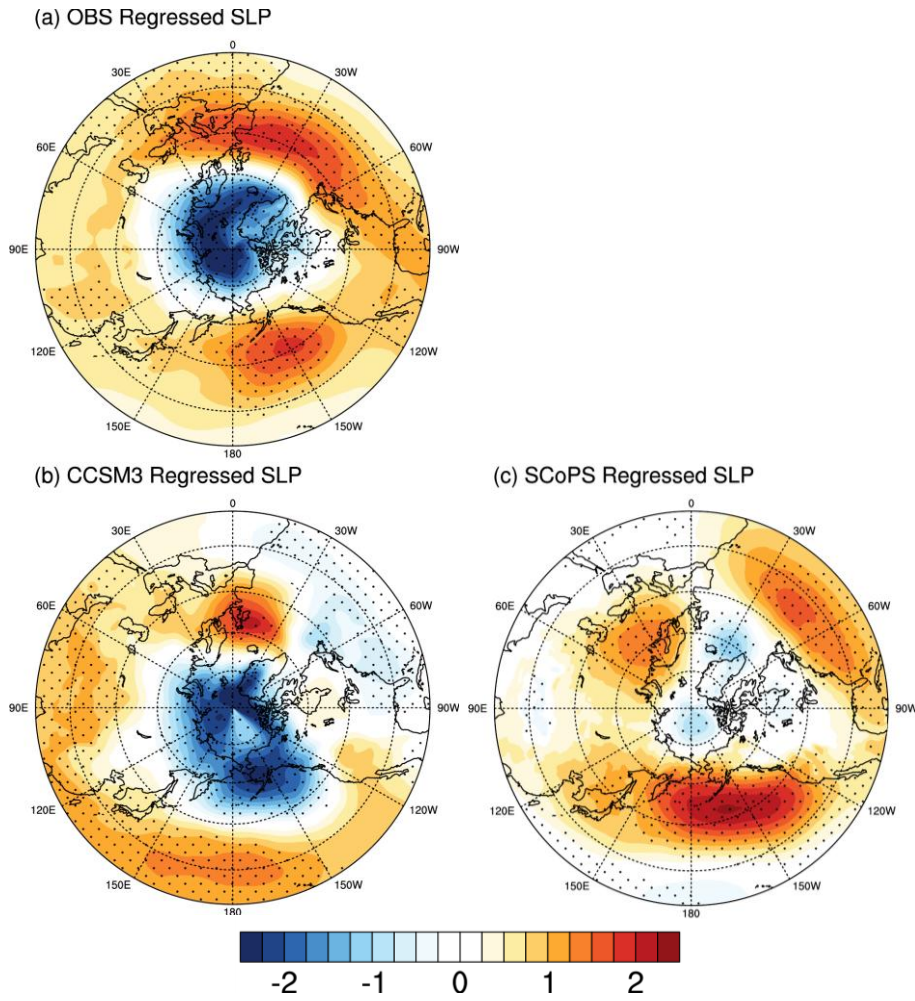


906

907

908 **Fig. 16.** Ensemble-averaged AO index from reanalysis (black), CCSM3  
909 (blue), and SCoPS (red). Filled areas indicate the results from all ensemble  
910 simulation for CCSM3 (blue) and SCoPS (red). Percentages in left bottom  
911 string indicate explained variance (averaged explained variance from each  
912 ensemble member) from the pattern.

913



915  
 916  
 917  
 918  
 919  
 920  
 921  
 922  
 923  
 924

**Fig. 17.** DJF mean sea level pressure anomaly regressed onto the leading PC for 1982–2013 from (a) reanalysis data, (b) CCSM3, and (c) SCoPS simulations with 1-month lead time.